Astronomical Journal, December 2002, in press

Hubble Space Telescope Evidence for an Intermediate-Mass Black Hole in the Globular Cluster M15— II. Kinematical Analysis and Dynamical Modeling[1]

Joris Gerssen, Roeland P. van der Marel
Space Telescope Science Institute, 3700 San Martin Drive, Baltimore, MD 21218

Karl Gebhardt
Astronomy Department, University of Texas at Austin, Mail Code C1400, Austin, TX 78712

Puragra Guhathakurta, Ruth C. Peterson[2]
UCO/Lick Observatory, Department of Astronomy and Astrophysics, University of California at Santa Cruz, 1156 High Street, Santa Cruz, CA 95064

Carlton Pryor
Department of Physics and Astronomy, Rutgers University, 136 Frelinghuysen Road, Piscataway, NJ 08854-8019

[1]Based on observations made with the NASA/ESA Hubble Space Telescope, obtained at the Space Telescope Science Institute, which is operated by the Association of Universities for Research in Astronomy, Inc., under NASA contract NAS 5-26555. These observations are associated with proposal #8262.

[2]Also at: Astrophysical Advances, Palo Alto, CA 94301.

ABSTRACT

We have used the Space Telescope Imaging Spectrograph (STIS) on the Hubble Space Telescope (HST) to obtain high spatial resolution spectroscopy of the central region of the dense globular cluster M15. The observational strategy and data reduction were described in Paper I (van der Marel et al. 2002). Here we analyze the extracted spectra with a cross-correlation technique to determine the line-of-sight velocities of individual stars. Our final STIS velocity sample contains 64 stars, two-thirds of which have their velocity measured for the first time. The new data set triples the number of stars with measured velocities in the central projected $R \leq 1''$ of M15 and doubles the number in the central $R \leq 2''$. We combine our data with existing ground-based data to obtain non-parametric estimates of the radial profiles of the projected rotation velocity, velocity dispersion, and RMS velocity $\sigma_{\rm RMS}$. The results differ from earlier work in the central few arcsec in that we find that $\sigma_{\rm RMS}$ rises to $\sim 14\,{\rm km\,s^{-1}}$, somewhat higher than the values of 10–12 $\rm km\,s^{-1}$ inferred previously from ground-based data.

To interpret the results we construct dynamical models based on the Jeans equation for a spherical system. If the velocity distribution is isotropic, then M15 must have a central concentration of non-luminous material. If this is due to a single black hole, then a fit to the full velocity information as function of radius implies that its mass is $M_{\rm BH} = (3.9 \pm 2.2) \times 10^3 {\rm M}_\odot$. The existence of intermediate-mass black holes in globular clusters is consistent with several scenarios for globular cluster evolution proposed in the literature. The inferred mass for M15 is consistent with the extrapolation of the relation between $M_{\rm BH}$ and $\sigma_{\rm RMS}$ that has been established for galaxies. Therefore, these results may have important implications for our understanding of the evolution of globular clusters, the growth of black holes, the connection between globular cluster and galaxy formation, and the nature of the recently discovered 'ultra-luminous' X-ray sources in nearby galaxies. Instead of a single intermediate-mass black hole, M15 could have a central concentration of dark remnants (e.g., neutron stars) due to mass segregation. However, we argue that the best-fitting Fokker-Planck models that have previously been constructed for M15 do not predict a central mass concentration that is sufficient to explain the observed kinematics. To fit the M15 data without any central dark mass concentration one must assume that the velocity distribution is significantly radially anisotropic near the center, which contradicts predictions from both Fokker-Planck and N-body calculations.

Subject headings: globular clusters: individual (M15) — stars: kinematics.

1. Introduction

The globular cluster M15 (NGC 7078) has one of the highest central densities of any globular cluster in our Galaxy. As a result, it has been one of the globular clusters for which the structure and dynamics have been most intensively studied in the past decade (as reviewed in van der Marel 2001). The present paper is the second in a series of two in which we present the results of a study with the Hubble Space Telescope (HST) of the line-of-sight velocities of stars in the central few arcsec of M15. Paper I (van der Marel et al. 2002) discussed the observations, and the extraction and calibration of the stellar spectra. In the present paper we determine the stellar line-of-sight velocities from the spectra, and we use the results to study the dynamics and structure of M15.

M15 is a proto-typical core-collapsed cluster (Djorgovski & King 1986; Lugger et al. 1987; Trager, King & Djorgovski 1995), with a stellar surface density profile that rises all the way into the center. Such clusters make up $\sim 20\%$ of all globular clusters in our Galaxy, and stand in marked contrast to King-model clusters, which show flat central cores and are modeled as tidally-truncated isothermal systems. Even imaging studies with HST have not provided any evidence for a homogeneous core in M15 (despite early claims to the contrary; Lauer et al. 1991). Guhathakurta et al. (1996) used the Second Wide Field and Planetary Camera (WFPC2) and found the projected surface number density profile inside $6''$ (0.34 pc) to be consistent with a power law $N(R) \propto R^{-0.82\pm0.12}$. Sosin & King (1997) used the Faint Object Camera (FOC) and obtained $N(R) \propto R^{-0.70\pm0.05}$ for turnoff stars. They also showed that the distributions for stars of different masses have slightly different power-law slopes, which is qualitatively consistent with the mass segregation predicted in a cluster in which two-body relaxation has been important.

Bahcall & Wolf (1976, 1977) constructed detailed models for the equilibrium stellar density distribution of a globular cluster in which a central black hole (BH) has been present for much longer than the two-body relaxation time. For a cluster of equal-mass stars one expects $N(R) \propto R^{-3/4}$, in surprisingly good agreement with the observed star count profile for M15. While BHs have been convincingly detected in the centers of galaxies (e.g., Kormendy & Gebhardt 2001), no convincing detections exist for globular clusters. On the other hand, few, if any, previous studies have had sufficient sensitivity to unambiguously detect BHs in globular clusters with masses $M_{\rm BH} \lesssim 5 \times 10^3\,{\rm M}_\odot$. There are many ways in which globular cluster evolution at high densities can lead to the formation of a massive BH in the center (Rees 1984). For example, core collapse induced by two-body relaxation may lead to sufficiently high densities for individual stars or stellar-mass black holes to interact or collide, with a single massive BH as the likely end product (Sanders 1970; Quinlan & Shapiro 1987, 1990; Lee 1987, 1993, 1995). Studies of such scenarios have gained much interest lately (Miller & Hamilton 2002; Mouri & Taniguchi 2002; Portegies Zwart & McMillan 2002) after the discovery of intermediate luminosity X-ray objects in external galaxies (e.g., Colbert & Mushotzky 1999). The emission of these objects may be due to accretion onto intermediate mass BHs. However, this interpretation is not uniquely implied by the data and there is no unique association of these objects with star clusters (e.g., Zezas & Fabbiano 2002).

While the observed star count profile of M15 is consistent with the presence of a BH, it can be explained equally well as a result of core-collapse (Grabhorn et al. 1992). Hence, the star count profile by itself yields only limited insight. An additional problem is that photometric studies

cannot determine whether light follows mass, and what the abundance and distribution of dark remnants are. Kinematical studies are therefore essential to gain further insight. Integrated light measurements of M15 initially suggested a very high central dispersion, $\sigma = 25 \pm 7\,\mathrm{km\,s^{-1}}$. This was a sharp increase from the dispersions of 5–15 $\mathrm{km\,s^{-1}}$ found at larger radii from the radial velocities of individual stars, which was interpreted as evidence for the presence of a $10^3\,\mathrm{M_\odot}$ central BH (Peterson, Seitzer & Cudworth 1989). This pioneering work spurred a lot of interest in globular cluster dynamics. However, all subsequent studies were unable to confirm the high central velocity dispersion measurement. In particular, it became clear that that the weighting of stars by their brightness in an integrated-light spectrum produces a large systematic uncertainty in the velocity dispersion deduced from the broadening of lines (Zaggia, Cappaccioli, & Piotto 1993; Dubath et al. 1994). Velocity measurements of individual stars are therefore called for.

Line-of-sight velocities are now known from ground-based studies for ~ 1800 M15 stars, as compiled by Gebhardt et al. (2000a). Many different studies contributed to this dataset, as reviewed in the introduction of Paper I. The projected velocity dispersion profile increases monotonically inwards from $\sigma = 3 \pm 1\,\mathrm{km\,s^{-1}}$ at $R = 7$ arcmin (Drukier et al. 1998), to $\sigma = 11 \pm 1\,\mathrm{km\,s^{-1}}$ at $R = 24''$. The analysis of Gebhardt et al. (2000a) suggested that the velocity dispersion is approximately constant at smaller radii, and is $\sigma = 11.7 \pm 2.8\,\mathrm{km\,s^{-1}}$ at the innermost available radius $R \approx 1''$. Outside of the very center, the velocity dispersion profile is well fitted by a spherical dynamical model with an isotropic velocity distribution and a constant mass-to-light ratio $\Upsilon = 1.7$ (in solar V-band units). However, this model underpredicts the velocity dispersion in the central 2 arcsec. The fit can be improved by addition of a central black hole, which causes the velocity dispersion to rise in Keplerian fashion as $\sigma \propto R^{-1/2}$ towards the center of the cluster. The best fit was obtained with a mass $M_{\mathrm{BH}} \approx 2 \times 10^3\,\mathrm{M_\odot}$ (Gebhardt et al. 2000a). However, the ground-based M15 velocity dispersion data can be fitted equally well with a model in which the mass-to-light ratio $\Upsilon(r)$ of the stellar population increases inwards to a value of ~ 3 in the center. This would not *a priori* be implausible, since mass segregation would tend to concentrate heavy dark remnants to the center of the cluster. Models with an anisotropic velocity distribution may even be able to fit the data with constant mass-to-light ratio and without a central black hole. Higher spatial resolution data and more detailed modeling are necessary to decide amongst these scenarios; this is the focus of the present series of papers.

It has been known for some time (Gebhardt et al. 1994) that M15 has a net projected rotation amplitude of $V_{\mathrm{rot}} \approx 2\,\mathrm{km\,s^{-1}}$ at radii comparable to the half-light radius (about 1 arcmin). More recent work (Gebhardt et al. 2000a; these results were also suggested by the integrated-light measurements of Peterson 1993) has revealed that the rotation amplitude is larger at small radii: $V_{\mathrm{rot}} = 10.4 \pm 2.7\,\mathrm{km\,s^{-1}}$ for $R \leq 3.4''$, implying that $V_{\mathrm{rot}}/\sigma \approx 1$ in this region. This large amplitude is surprising because two-body relaxation should rapidly transfer net angular momentum outward from such small radii (see the discussion in Gebhardt et al. 2000a). Even more surprising is that the position angle of the projected rotation axis at small radii is $\sim 100^\circ$ different from that near the half-light radius. Although the large increase in the rotation amplitude at small radii may have something to do with the presence of a central BH (Gebhardt et al. 2000a), the increase and change in position angle are not predicted by any current theory of globular cluster dynamical evolution.

Phinney (1993) used an alternative argument to constrain the mass distribution of M15. There are two millisecond pulsars in M15 at a distance $R = 1.1''$ from the cluster center that have a negative period derivative $\dot{P}$. This must be due to acceleration by the mean gravitational field of the cluster, since the pulsars are expected to be spinning down intrinsically (positive $\dot{P}$). The observed $\dot{P}$ values place a strict lower limit on the mass enclosed within a projected radius of $R = 1.1''$. Combined with the observed light profile this implies that the mass-to-light ratio must increase centrally inwards. A similar pulsar acceleration study was recently performed by d'Amico et al. (2002) for the cluster NGC 6752, which suggests a central increase in mass-to-light ratio in this cluster as well. For M15, Phinney (1993) obtained $\Upsilon > 2.1$ for the total mass-to-light ratio within $R \leq 1.1''$, with a statistically most likely value of $\Upsilon \approx 3.0$. These results are consistent with the analysis of stellar kinematics (see also Dull et al. 1997). Unfortunately, the pulsar data, like the ground-based observations of the kinematics, does not constrain the distribution of mass tightly enough to discriminate between the effects of mass segregation and a central BH.

Tighter constraints on the distribution of mass near the center of M15 need observations of the kinematics with better angular resolution than previous studies and observations from space can supply these. So we started a project to use HST to determine more stellar velocities close to the center of M15 (HST program GO-8262, PI: van der Marel). As described in Paper I, we used the Space Telescope Imaging Spectrograph (STIS) to obtain observations with the $0.1''$-wide slit at 18 adjacent positions near the cluster center. All spectra cover the wavelength range from 5073–5359Å, which includes the Mg b triplet at ~ 5175Å. The resolution is 0.276Å per pixel, which corresponds to $15.86\,\mathrm{km\,s^{-1}}$. Extensive reductions and calibrations were performed to extract spectra with signal-to-noise ratio $S/N > 5.5$ per pixel for a total of 131 stars. The velocity calibration of the spectra was the most crucial and difficult aspect of the data reduction. Corrections were necessary for: drifts in the wavelength scale during an orbit; changes in the velocity of HST as it orbits the Earth; and wavelength shifts induced by the offsets of stars from the center of the slit. The analyses in Paper I indicate that the uncertainty in velocity scale caused by residual calibration errors in the final spectra is $\sim 2.5\,\mathrm{km\,s^{-1}}$.

Here we analyze the 131 stellar spectra from Paper I, and we show that for 64 of them the quality is sufficient to obtain an accurate line-of-sight velocity measurement. We use the results to obtain new constraints on the dynamics and structure of M15. The paper is organized as follows. In Section 2 we describe the cross-correlation algorithm that we have used for the extraction of line-of-sight velocities, including the choice of spectral templates. We discuss the reliability of the results based on an analysis of our STIS observations of a calibration star. In Section 3 we describe the application of the cross-correlation algorithm to the STIS spectra of M15. We describe how we have corrected the inferred velocities for the effects of crowding and blending. The reliability of the inferred velocities is verified by comparison to ground-based data, for those stars for which the latter are available. In Section 4 we infer the velocity dispersion and rotation velocity profiles of M15 from the combined HST and ground-based line-of-sight velocity samples. In Section 5 we present dynamical models to interpret the results, and we discuss the implications for the dynamical structure and mass distribution of M15. Section 6 discusses and summarizes the main conclusions.

2. Extraction of Line-of-Sight Velocities

2.1. Algorithm

Extracting line-of-sight velocities from stellar absorption line data is usually accomplished by cross-correlating the spectral data with a template spectrum of known velocity. One of the most widely used implementations of the cross-correlation method has been developed by Tonry and Davis (1979). Several non cross-correlation based methods have also been developed in the past two decades. While these methods are better suited to extract the full line-of-sight velocity distributions from absorption line spectra, they do so at the cost of requiring high signal-to-noise ratio spectra. For the STIS data analyzed here, the only kinematical quantity of interest is the line-of-sight velocity. These data are thus best suited to a cross-correlation based analysis.

To this end, all line-of-sight velocities were derived in IRAF using the task XCSAO. XCSAO is part of the RVSAO package described extensively in Kurtz & Mink (1998). XCSAO is essentially a refined and updated version of the cross-correlation algorithm developed by Tonry & Davis (1979). XCSAO is a well-tested and often used task with many attractive features. It provides a handle on both the confidence and the error of a particular velocity measurement by means of the r statistic, developed originally by Tonry & Davis (1979), which we refer to here as $r_{\rm cc}$ (in essence, this statistic measures the amplitude of the cross-correlation peak, divided by the amplitude of the 'average' peak expected from noise and template mismatch). Following Kurtz & Mink (1998), we chose to calibrate this statistic empirically (see below). Another useful feature of XCSAO is its batch mode option which considerably simplifies the task of having to analyze large numbers of spectra (our STIS data set consists of 19200 apertures).

All spectra were reduced and wavelength calibrated with an adaptation of the STIS reduction pipeline as described in Paper I. Before the actual cross-correlation takes place, XCSAO performs the following tasks: continuum removal, apodization and Fourier filtering. Due to undersampling of the line spread function (see Paper I) the STIS spectra are strongly undulated, i.e. there are low frequency flux variations with wavelength that are not related to the intrinsic continuum distribution. To roughly preserve the correct line ratios, the continuum was removed by division rather than by subtraction. The ends of the spectra were cosine tapered to avoid aliasing. Finally, a Fourier bandpass filter was applied to remove both the low frequencies (residual continuum variations) and the high frequencies (noise). The software then calculates the cross-correlation function and finds the strongest peak in a $200\,{\rm km\,s^{-1}}$ range centered on the systemic velocity of M15 ($-107.5\,{\rm km\,s^{-1}}$). The position of this peak is fitted with a parabolic function to derive the velocity and its formal random error.

2.2. Spectral Templates

The strength of a cross-correlation peak depends largely on how well the template spectrum matches the observed spectrum. Template spectra were therefore obtained of a cluster star at 40 arcsec from the center of M15, which was also used for target acquisition purposes (see Paper I).

This star is a very bright giant and relatively high signal-to-noise spectra were therefore readily obtained. This ensures that uncertainties in the inferred velocities result mainly from the noise in the M15 data and are not associated with the template (save template mismatch).

Templates observed with the same instrumental setup as the science observations have the advantage that the instrumental signature will be similar in both spectra. Any instrumental effect can therefore be easily calibrated out. However, the largest instrumental effect is usually a broadening of the cross-correlation function due to instrumental broadening of the absorption lines. This does not influence the position of the cross-correlation peak and, hence, does not affect velocity measurements.

In addition to the observed templates, a number of artificial templates were created based on Kurucz models. A grid of 30 model stellar atmospheres with varying temperatures (4000K to 8000K), metallicities (-2.1 dex to -2.5 dex) and surface gravities ($\log g$ from 0.5 to 2.0) covering a wavelength range from 5000 to 5500 Å were calculated. The metallicity range was chosen to bracket the current best estimate of M15's metallicity.

Artificial templates have the benefit of having infinite signal-to-noise ratios and they can be constructed to closely match the spectral features of the M15 data. They lack the instrumental signature, but as noted above, this would mainly affect measurements of the velocity dispersion (i.e., the line widths) which is irrelevant to the data presented here.

2.3. Reliability of the Line-of-Sight Velocities

In order to successfully attain our goal of measuring the stellar velocity dispersion within the central arcseconds of M15, several intricate corrections to the derived line-of-sight velocities had to be made. These corrections stem from the motion of HST (which has an orbital velocity of $7.5\,\mathrm{km\,s^{-1}}$) and the fact that the stars generally do not fall in the center of the slit (the full width of the slit corresponds to $26.5\,\mathrm{km\,s^{-1}}$ in the dispersion direction). To calibrate the necessary corrections, 14 short exposure spectra of the bright field star HD 122563 (F8IV, magnitude $V = 6.2$) were obtained at offset positions parallel and perpendicular to the slit. Both the corrections and the calibration are described fully in Paper I. In the remainder of this paper it should be implicitly understood that these corrections were applied to all velocities. The star HD 122563 was chosen because its low metallicity, [Fe/H] $= -2.65 \pm 0.2$ (Sneden & Parthasarathy 1983), which is close to the metallicity of M15, [Fe/H] ≈ -2.22 (Harris 1996).

An additional use of the two-dimensional long-slit data obtained for HD 122563 is to calibrate the confidence limits on the results obtained with the XCSAO cross correlation software. In each of the 14 long-slit spectra we extracted 21 one-dimensional spectra at different positions along the slit. This yielded 294 spectra, each for a $0.1'' \times 0.1''$ aperture placed somewhere within $1.0''$ from the position of the star on the sky. Because of the wings of the PSF, each of these spectra contains a meaningful amount of light from the star. For each of these 294 spectra the line-of-sight velocities and the errors were derived using the cross-correlation routine XCSAO. In addition, the r_{cc} statistic was derived, as well as the average signal-to-noise ratio S/N per pixel (determined

from the error frames delivered by the HST/STIS pipeline). All apertures were correlated against all Kurucz model templates and also against the acquisition star template. The results were found not to change significantly from template to template. This is most likely due to the rather limited wavelength range of the observed spectra, 250 Å. In the end we adopted the template which yielded the marginally highest value of $r_{\rm cc}$.

The inferred velocities were used to empirically calibrate the confidence limits in a manner analogous to Kurtz & Mink (1998). The left panel of Figure 1 shows the logarithm of the absolute difference between the measured line-of-sight velocity and the literature value of the velocity of HD 122563 versus the $r_{\rm cc}$ statistic. A clear break in the distribution of points occurs at $r_{\rm cc} \approx 2.5$. For $r_{\rm cc} \gtrsim 2.5$ all velocity differences are only a few $\mathrm{km\,s^{-1}}$ and are thus considered reliable. Not surprisingly, for small values of $r_{\rm cc}$ the inferred velocities become unreliable. As an additional test of the reliability we have constructed a similar diagram showing the logarithm of the absolute velocity difference versus the signal-to-noise ratio (right panel of Figure 1). This plot shows the same qualitative behavior as the $r_{\rm cc}$ statistic plot. It suggests that reliable velocities are derived for an average S/N $\gtrsim 5$ per pixel.

An optimal selection of the $r_{\rm cc}$ and S/N cutoff limits can be made by applying both criteria simultaneously. Imposing a lower limit on $r_{\rm cc}$ of 2.0 (vertical line in the left panel) would include very deviant points. However, all of the deviant points have S/N values smaller than 5.5 (these points are shown as filled circles in the left panel of Figure 1). A similar situation is encountered in the right panel, where all the deviant points that are beyond the S/N cutoff, S/N $\gtrsim 5.5$, have unacceptable $r_{\rm cc}$ values (again shown as filled circles). Thus, in both panels all points that are to the right of their adopted cutoffs and are shown as open circles are considered acceptable. With the adopted values of $r_{\rm cc} = 2.0$ and S/N = 5.5, no deviant points remain while the number of reliably measured velocities is maximized. Extending the $r_{\rm cc}$ and S/N cutoffs downward as far as possible is by no means critical for the calibration star itself but in M15 the number of reliably measured stars is at a premium. Kurtz & Mink (1998) generally use more conservative values of $r_{\rm cc}$. However, they do not apply the $r_{\rm cc}$ statistic and the S/N criterion simultaneously to their data.

The additional checks discussed below also indicate that the values adopted here yield reliable results for our STIS setup.

3. Kinematical Results

3.1. Raw Stellar Velocities

As described in Paper I, the STIS data set allowed the extraction of (one-dimensional) spectra with $S/N > 5.5$ for a total of 131 stars in M15. We analyzed each of the extracted one-dimensional spectra with the cross-correlation algorithm described in Section 2. Based on the analysis of the calibration star discussed in Section 2, we expect that the inferred velocities are reliable for all spectra that yield a cross-correlation statistic $r_{\rm cc} > 2$. As a sanity check, we plot in Figure 2 the quantity $(v - v_{\rm sys})/\sigma$ as a function of $r_{\rm cc}$. Here $v_{\rm sys} \approx -107.5\,\mathrm{km\,s^{-1}}$ is the systemic heliocentric

velocity of M15 and $\sigma \approx 12\,\mathrm{km\,s^{-1}}$ is a rough estimate of the stellar velocity dispersion near the center (Gebhardt et al. 2000a). This figure is analogous to Figure 1. It shows that there are no inferred velocities with $r_{\rm cc} > 2$ that are implausible in view of our understanding of the kinematics of M15. So there seems no reason to mistrust any of the inferred velocities with $r_{\rm cc} > 2$, which confirms the results from the calibration star analysis.

The STIS data yield a reliable velocity result (i.e., $S/N > 5.5$ and $r_{\rm cc} > 2$) for 64 of the 131 extracted one-dimensional spectra. According to the prescription of Paper I, the 131 extracted spectra were constructed by combining one or more apertures. It makes essentially no difference, however, whether the velocities are derived directly from these co-added spectra, or whether they are derived by averaging the velocities of individually analyzed apertures. The 64 selected stars are listed in Table 1. We will refer to this sample as our 'STIS velocity sample'. The identification number in the first column corresponds to the entry number in the HST/WFPC2 stellar catalog described and presented in Paper I. The inferred heliocentric velocity $v_{\rm obs}$ is listed in column 6, and its error $\Delta v_{\rm obs}$ in column 7. These are the 'raw' velocities inferred from the spectra, which are not yet corrected for blending. Blending corrections are discussed in Section 3.3 below. The velocity error $\Delta v_{\rm obs}$ listed for each star is the quadratic sum of the formal error of the cross-correlation result and the spectral velocity calibration uncertainty. For the latter we adopted a value of $2.5\,\mathrm{km\,s^{-1}}$, based on the results and discussion of Paper I. The analysis of the calibration star data shown in Figure 1 confirms that there there are no systematic uncertainties in the data that exceed this value.

Figure 3 shows the color-magnitude diagram (CMD) of M15 for the stars in the HST/WFPC2 catalog discussed in Paper I. The stars in the STIS velocity sample are highlighted. These stars generally have a magnitude in V brighter than 18.5, although there is one star that is as faint as $V = 19.05$. Red giant and sub-giant stars dominate the sample. This is true not only because their number density is higher than for bluer horizontal branch stars, but also because blue stars often lack sufficiently strong stellar absorption lines to yield a strong cross-correlation peak (Mayor 1980). Two stars in the STIS velocity sample (ID numbers 3393 and 5846; encircled crosses in Figure 3) occupy a location close to the instability strip and are probably RR Lyrae variables. RR Lyrae stars are velocity variables that can have velocity excursions of $\pm 50\,\mathrm{km\,s^{-1}}$ from the mean (Smith 1995). We therefore exclude these two stars from our subsequent dynamical analysis.

The distance d of the stars in the STIS velocity sample from the cluster center ranges from 0.2 to 27 arcsec. The adopted position of the cluster center is given in Paper I, and is based on the analysis of Guhathakurta et al. (1996). The influence of the uncertainty in this position ($0.2''$ in each coordinate) on the results of our study is negligible, as discussed in Section 5.3. The solid line in the left panel of Figure 4 shows a histogram of the distribution of the stars in the STIS velocity sample with distance. For comparison, the dashed line shows the distribution of the stars for which a velocity determination (with an uncertainty better than $10\,\mathrm{km\,s^{-1}}$) was known from ground-based data (Gebhardt et al. 2000a). The logarithm of their corresponding cumulative distributions are shown in the right panel. The heavy solid line in this panel shows the distribution for the combined STIS and ground-based velocity samples. It is clear that the STIS data significantly increase the number of stars with known velocities close to the cluster center. Figure 5 shows the spatial distribution in the central $4'' \times 4''$ of the stars with known line-of-sight

velocities.

3.2. Consistency Checks

About one third of the stars in the STIS velocity sample also have a ground-based measurement of the line-of-sight velocity (Gebhardt et al. 2000a). A comparison of the ground-based velocities to the HST/STIS velocities is shown in Figure 6. The agreement is generally excellent, which confirms the reliability of the HST results. The residual velocities ($v_{\rm HST} - v_{\rm ground}$) are shown in Figure 7 as a function of V-band magnitude and $B-V$ color. There are no trends with either, which once more validates the velocities determined with STIS. The weighted mean residual velocity is $0.2 \pm 1.4\,{\rm km\,s^{-1}}$, indicating that our velocity zero point is consistent with what has been inferred from ground-based observations. The χ^2 value is 29.1 for 23 points, which is statistically acceptable.

Neither the HST velocities nor the ground-based velocities in Figure 6 contain an explicit correction for blending[3]. However, even the best ground-based data (Gebhardt et al. 2000a) has a poorer PSF than the HST data, so some of the small discrepancies seen in Figure 6 may be due to the effects of blending. This is true in particular for the two labeled stars in Figure 6, which appear to lie somewhat offset from the one-to-one relation. The first star, ID 5222, is close ($\sim 0.1''$) to another star and it is possible that the ground-based determination of its velocity is more strongly affected by blending than the HST measurement. The second star, ID 5831, is a member of the triple star system AC 214 that is located within $0.5''$ of the M15 center. Its three $V \approx 15.5$ members are separated by about $0.1''$. Our STIS sample contains the velocities of two of AC 214's members (ID 5831 and ID 5846). We were unable to extract a reliable velocity for the bluest of the three stars (ID 5872, $B-V = 0.02$). Interestingly, for ID 5831 and ID 5846 we find a velocity difference of $\sim 50\,{\rm km\,s^{-1}}$. This provides a tantalizing hint for the existence of a central compact object in the midst of AC 214. However, ID 5846 is a possible RR Lyrae variable and the measured velocity difference is consistent with the maximum velocity excursion of an RR Lyrae variable. The ground-based measurement ($-116\,{\rm km\,s^{-1}}$, Gebhardt et al. 2000a) of ID 5831 is consistent with being the weighted mean of the two values inferred from the HST/STIS data. The ground-based measurement therefore probably suffered from blending of light with ID 5846.

In addition to the comparison with ground-based results, we have also performed internal consistency checks on the STIS data set. As described in Paper I, the observational strategy yielded several independent spectra for most stars. These independent spectra correspond either to different rows in the same exposure (i.e., adjacent positions along the slit for a given slit position) or to different exposures (i.e., adjacent slit positions on the sky, observed either within the same telescope visit to the target or in different visits). The strategy adopted for our final results has been to co-add spectra for a given star, and to analyze the grand-total summed

[3]The ground-based velocities cannot easily be corrected for blending. So when comparing the ground-based velocities to the HST velocities it makes sense to use HST velocities that are not corrected for blending either. In the subsequent dynamical analysis we do correct the HST velocities for blending, as described in Section 3.3 below.

spectrum. However, for testing we have also performed a cross-correlation analysis of all 19,200 individual spectra in our dataset. We extracted those results that conform to the selection criteria with respect to blending, S/N and $r_{\rm cc}$ that were discussed previously. For many stars in our STIS velocity sample this yields two or more independent velocity measurements. Let v_i and v_j be two independent velocity measurements for the same star, and let Δv_i and Δv_j be the corresponding uncertainties. One then expects each difference $\Delta v_{ij} \equiv v_i - v_j$ to be a Gaussian random deviate drawn from a distribution with zero mean and dispersion $\epsilon_{ij} \equiv [(\Delta v_i)^2 + (\Delta v_j)^2)]^{1/2}$. Figure 8 shows a histogram of all the Δv_{ij}. It includes those stars for which multiple independent measurements could be extracted; each star can appear many times in the histogram, depending on how many different measurements are available. The histogram is well fit by a Gaussian with a dispersion of $6\,{\rm km\,s^{-1}}$ (solid curve). This is in reasonable agreement with the expected value of $5\,{\rm km\,s^{-1}}$, based of the average of the individual uncertainties ϵ_{ij}. This implies that there is no reason to suspect the presence of unidentified systematic errors in the analysis, consistent with the results from the comparison of STIS and ground-based results.

3.3. Statistical Corrections for Blending

Even with the resolution of HST, the light profiles of stars in the densely populated central region of M15 overlap partially with neighboring stars. So when the spectrum of an individual star is extracted from our HST/STIS data set, only a fraction f of the total light is actually due to the star of interest. The remaining fraction $(1 - f)$ is due to 'contaminating' stars. The algorithm for spectral extraction employed in Paper I was designed to yield values $f \geq 0.75$. We verified that the main results of our analysis are insensitive to the exact choice of this cut (see also Section 4 below). The fraction f is listed in Table 1 for each spectrum that was analyzed. The blending fraction $(1 - f) \leq 0.25$ is small, but does need to be corrected for.

To correct for blending we note that the observed velocity $v_{\rm obs}$ (the velocity extracted from the one-dimensional spectrum using cross-correlation) is, to a good approximation, equal to the luminosity weighted mean velocity of all the light that contributes to the spectrum. Therefore,

$$v_{\rm obs} = f v_{\rm star} + (1 - f) v_{\rm cont}, \tag{1}$$

where $v_{\rm star}$ the velocity of the star of interest, and $v_{\rm cont}$ is the luminosity weighted mean velocity of the contaminating stars. The analysis of Paper I tells us which stars are contaminating the spectrum and what fraction of the light they contribute. However, we do not generally know the velocities of the contaminating stars. On the other hand, we do know something about the contaminating stars: they belong to the cluster. Hence, the velocities of the contaminating stars are random deviates drawn from the line-of-sight velocity distribution of the cluster. The expectation value of the statistical quantity $v_{\rm cont}$ is therefore equal to $v_{\rm sys}$. The dispersion is equal to $A\sigma$, where σ is the line-of-sight velocity dispersion of the cluster at the position of interest. The constant $A \leq 1$ depends on the number of stars that provide the contaminating light. If there is only a single star, then $A = 1$. Upon taking the first and second moments of equation (1) we can calculate the expectation value of $v_{\rm star}$, which we denote v_*, and the dispersion of $v_{\rm star}$, which we

denote Δv_*. This yields

$$v_* = v_{\rm sys} + \frac{1}{f}[v_{\rm obs} - v_{\rm sys}], \qquad \Delta v_* = \frac{1}{f}[(\Delta v_{\rm obs})^2 + (1-f)^2 A^2 \sigma^2]^{1/2}, \tag{2}$$

where $\Delta v_{\rm obs}$ is the formal error of the velocity inferred from the observed spectrum through cross-correlation. In the following we assume that $A = 1$; this is conservative in the sense that it yields the largest uncertainty Δv_*.

The quantities v_* and Δv_* are the final estimate of the stellar velocity and its error. They result from correcting the measurement $v_{\rm obs}$ and its error $\Delta v_{\rm obs}$ for blending. The accuracy of these corrections was verified through Monte-Carlo simulations. Equation (2) shows that the correction is such that it increases the deviation of the stellar velocity from the cluster mean by a factor $1/f$. This is because blending will, on average, tend to draw measured velocities towards the cluster mean. Equation (2) also shows that the error Δv_* of the corrected velocity is larger than the error $\Delta v_{\rm obs}$ of the measured velocity. This is so because of our poor knowledge of the velocities of the contaminating stars. The values of v_* and Δv_* are listed in Table 1 for all the stars in the STIS velocity sample. They do not depend sensitively on the exact choices of $v_{\rm sys}$ and σ, for which we adopted $v_{\rm sys} = -107.5\,{\rm km\,s^{-1}}$ and $\sigma = 12\,{\rm km\,s^{-1}}$ (Gebhardt et al. 2000a).

The median value of f in our velocity sample is 0.85. The uncorrected velocities have a median $|v_{\rm obs} - v_{\rm sys}|$ of $8.8\,{\rm km\,s^{-1}}$ and a median error $\Delta v_{\rm obs}$ of $3.8\,{\rm km\,s^{-1}}$. The corrected velocities have a $|v_* - v_{\rm sys}|$ of $11.0\,{\rm km\,s^{-1}}$ and a median error Δv_* of $5.4\,{\rm km\,s^{-1}}$. Thus, the blending corrections are always relatively small. This is because $(1-f)$ is always less than 25 percent; stars in our data set with larger amounts of blending simply did not make it into our final STIS velocity sample.

4. Rotation Velocity and Velocity Dispersion Profiles

The kinematical analysis of the data and the subsequent dynamical modeling benefit from having the largest possible sample. We have therefore combined the 64 stars in the STIS velocity sample with the 1777 stars in the ground-based sample used previously by Gebhardt et al. (2000a). There are 23 stars in common to both samples (see Table 1 and Figures 6 and 7). Those stars were assigned a velocity based on the weighted mean of the two measurements[4]. One could argue that the STIS velocities should be more accurate, so that it might be more appropriate to ignore the ground-based velocity measurements for these stars. However, since the HST and ground-based velocities are generally in good agreement (Figure 7), this doesn't affect any of our final results. Based on their locations in the CMD diagram, a total of 19 stars (including two in the HST sample) are possible RR Lyrae candidates. These stars were excluded from the sample, yielding a

[4]The 1-σ error in a weighted average of N measurements z_i is given by $[\sum_{i=1}^{N} 1/(\Delta z_i)^2]^{-1/2}$. However, this underestimates the true error if there are systematic errors in addition to Gaussian random errors. These cases manifest themselves by having a χ^2 that is larger than the number of degrees of freedom (where the χ^2 is defined to measures the residuals of the data with respect to their weighted average). In these cases we increased the errors to yield a χ^2 equal to the number of degrees of freedom.

final sample of 1797 stars.[5]

We have used two non-parametric techniques to estimate kinematical profiles from the discrete velocity measurements: LOWESS and SROTATE. These techniques yield the velocity dispersion and the amplitude and position angle of rotation, as functions of radius. LOWESS is a smoothing-based technique that uses a locally weighted regression algorithm, and is described fully in Gebhardt et al. (1994). It finds a smooth curve for the kinematical profiles as a function of radius. At each radius, it uses a fixed fraction of the data points in both radial directions. The data points are weighted depending on their distance from the radius of interest using an inverted parabolic function. The smoothing parameter is the fraction of the data included in the fit at any given radius, for which we generally use 10%. The kinematical parameters are estimated using a maximum likelihood estimator that includes both the uncertainties on the individual velocity measurements and their assigned weights. The statistical uncertainties on the inferred profiles are calculated using Monte Carlo simulation. An undesirable feature of LOWESS is that it tends to wash out small scale features, which can bias the kinematical profiles close to the center. This problem is circumvented by the technique SROTATE, which is described fully in Gebhardt et al. (2000a) (the technique is not referred to as SROTATE in that paper, but it is described in the fifth paragraph of its section 3.1). It is similar to LOWESS in most respects, and differs primarily in that it allows for a variable size of the data window (i.e., of the smoothing). At most radii, it used a fixed fraction of the data points in both radial directions, as does LOWESS. However, at the boundaries of the dataset the window size shrinks to a smaller number of data points, although no smaller than a preset 'minimum window size'. This approach preserves sharp radial variations close to the cluster center, while also maintaining the desirable feature of LOWESS of lessening large variations due to discrepant data points. The results described in the remainder of this section were all obtained with SROTATE and a minimum window size of 11 data points. The main features of the results were found not to depend sensitively on the exact choice of the minimum window size. As a check we also determined the kinematical profiles with LOWESS. Although the results from LOWESS are somewhat unreliable at the smallest radii, it did yield results that are statistically consistent with those derived from SROTATE. Overall, the kinematical profiles presented here are robust, and do not depend sensitively on either the choice of the analysis algorithm of the choice of the algorithm parameters.

Figure 9a–c show the radial profiles of the velocity dispersion σ, the rotation velocity $V_{\rm rot}$, and the position angle $\mathrm{PA_{kin}}$ of the kinematical major axis. The 68.3% confidence bands are indicated with dotted curves. At radii larger than a few arcsec the data set is dominated by stars with ground-based velocity measurements and, as a consequence, the results derived at these radii are almost identical to those obtained previously by Gebhardt et al. (2000a, their Figure 13). Therefore, the results at the smallest radii are of primary interest here. Gebhardt et

[5]We note that the ground-based velocities in the sample were not corrected for blending in the same way that the HST/STIS velocities were. This should not be a problem, because the ground-based velocities dominate the sample only at radii where crowding is less of a problem. We verified this with a number of tests, for example, by studying the kinematics inferred from stars of different magnitudes. From these tests we conclude that potential blending in the ground-based data does not affect the main conclusions of our paper at a significant level.

al. (2000a) found an increase in the rotation velocity of M15 towards the center of the cluster, with a maximum of $V_{\rm rot} \approx 10\,{\rm km\,s^{-1}}$ at a radius $R \approx 2.5''$. We find that the rotation velocity actually continues to rise inward to a value of $V_{\rm rot} \approx 13\,{\rm km\,s^{-1}}$ at our innermost (trustworthy) radius, $R \approx 0.5''$. The velocity dispersion σ shows a mild inwards decrease at small radii, from $\sigma \approx 14\,{\rm km\,s^{-1}}$ at $R \approx 4''$ to $\sigma \approx 10\,{\rm km\,s^{-1}}$ at $R \approx 0.5''$. This is the same radial range over which the rotation velocity shows a strong inwards increase. The value of $\rm PA_{kin}$ appears to decrease by $\sim 50^\circ$ when going inward from $R \approx 4''$ to $R \approx 0.5''$, but this decrease is only marginally significant. The fact that $V_{\rm rot}/\sigma \approx 1$ near the center of M15 is quite surprising. This implications of this were already discussed at length by Gebhardt et al. (2000a), and we will therefore not comment further on it here.

The pressure in a stellar system is determined by the mean squared velocity of the stars (Binney & Tremaine 1987). In hydrostatic equilibrium, the pressure gradient balances the gravitational force. The quantity that is of primary importance from a dynamical point of view is therefore neither $V_{\rm rot}$ nor σ, but the mean squared projected line-of-sight velocity $V_{\rm rot}^2 + \sigma^2$. We define $\sigma_{\rm RMS}(R) \equiv \langle V_{\rm rot}^2 + \sigma^2 \rangle^{1/2}$, where the angle brackets denote the average over a ring of radius R on the projected plane of the sky. The most convenient way to determine $\sigma_{\rm RMS}$ from the discrete velocity measurements is to use `SROTATE` while keeping the rotation velocity fixed at zero. The resulting profile is shown in Figure 9d. Figure 10 is similar, but for visualization purposes it also shows the individually measured stellar velocities for comparison. The quantity $\sigma_{\rm RMS}$ measures the spread among these individual velocities (properly corrected for the small contribution from measurement uncertainties). The uncertainty in the determination of $\sigma_{\rm RMS}$ scales as the inverse square-root of the number of data points, and is at all radii much smaller than $\sigma_{\rm RMS}$ itself. Outside the central few arcsec, the data are dominated by stars with ground-based velocity measurements and the $\sigma_{\rm RMS}$ profile is almost identical to that inferred by Gebhardt et al. (2000a). However, at smaller radii our results are more accurate because of the addition of velocity measurements from HST. We find that $\sigma_{\rm RMS}$ increases from $\sim 10\,{\rm km\,s^{-1}}$ at $R = 10''$ to $\sim 14\,{\rm km\,s^{-1}}$ at $R = 3''$. Inside of the central few arcsec $\sigma_{\rm RMS}$ is consistent with being constant at $\sim 14\,{\rm km\,s^{-1}}$. This exceeds the central values of 10–12 $\rm km\,s^{-1}$ inferred by Dull et al. (1997) and Gebhardt et al. (2000a).

In our analysis we have included only those STIS spectra for which a single star contributes a fraction f of the total light that exceeds $f_{\rm min} = 0.75$. If one chooses a more stringent limit, then the number of stars for which velocities can be determined decreases. For example, if one uses $f_{\rm min} = 0.90$, then the size of the STIS velocity sample reduces to only 22 stars (see Table 1). On the other hand, these stars are the ones for which the measurements are most secure. It is therefore a useful test to check that the results for these stars are consistent with the results for the sample as a whole. The STIS velocity sample contains 13 stars with $f \geq 0.90$ that reside at $R \leq 6''$ from the M15 center. These stars have an average distance from the cluster center $\langle R \rangle = 3.3''$ and their RMS projected line-of-sight velocity is $\sigma_{\rm RMS} = 14.1 \pm 3.2\,{\rm km\,s^{-1}}$. This is in excellent agreement with the results obtained from the full sample, shown in Figure 9d. This indicates that main results of our study do not depend significantly on either the amount of blending allowed during the extraction of the STIS spectra (see Paper I) or the subsequent

blending corrections (see Section 3.3).[6]

To assess the implications of our new observational results we proceed in Section 5 by constructing detailed dynamical models. As discussed below, these models use a maximum likelihood approach that operates directly on the individually observed stellar velocities. This has the advantage that there is no dependence on arbitrary binning or smoothing parameters, such as the data window size in `SROTATE`. Nonetheless, the kinematical profiles in Figure 9 are important for providing insight into both the dynamical state of M15 and the results of the likelihood analysis (although the profiles are not themselves used in the dynamical modeling).

5. Dynamical Modeling

5.1. Formalism

To determine the mass distribution in M15 we assume that the cluster is spherical and that it is in hydrostatic equilibrium. The assumption of sphericity is adequate because the isodensity contours of M15 are not far from circular, at least at the small radii that are of primary interest here (Guhathakurta et al. 1996). The assumption of hydrostatic equilibrium is also adequate, despite the fact that a cluster like M15 undergoes secular evolution as a result of two-body relaxation. The two-body relaxation time significantly exceeds the dynamical time and the evolution therefore proceeds through a series of states that are all approximately in hydrostatic equilibrium. A spherical system in hydrostatic equilibrium obeys the Jeans equation (Binney & Tremaine 1987):

$$\frac{1}{\rho}\frac{d(\rho\sigma_r^2)}{dr} + \frac{2\beta\sigma_r^2}{r} + \frac{d\Phi}{dr} = 0. \tag{3}$$

Here ρ is the mass density, Φ is the gravitational potential, $\beta \equiv 1 - \sigma_t^2/\sigma_r^2$ is a measure of the anisotropy of the stellar velocity distribution, and σ_r^2 and σ_t^2 are the mean-squared velocities in the radial and tangential directions, respectively. In general, all these quantities are a function of the three-dimensional radius r. Note that the assumption of sphericity does not imply that rotation is fully ignored. It is possible to construct spherical dynamical models that rotate. Rotation contributes to the mean-squared velocities in the azimuthal direction, and therefore is included in equation (3). So while we do not model the rotation of M15 explicitly, we do include its contribution to the hydrostatic support.

At a given position in three-dimensional space, the mean-squared velocity in the direction

[6]The algorithm of Paper I that constructs a grand-total spectrum for each star has more parameters than just $f_{\rm min}$ (although $f_{\rm min}$ is certainly the most important one). For example, an individual aperture is rejected in the construction of the grand-total spectrum for a star if that star does not contribute at least a fraction $g > g_{\rm min} = 0.5$ of the light in the aperture. As for $f_{\rm min}$, the results of our analysis are not sensitive to the precise choice of $g_{\rm min}$. The reason for this is that most of the light in the final grand-total spectrum for each star always comes from apertures with $g \gtrsim f_{\rm min}$ (otherwise it would not be possible for the sum of the aperture spectra to have $f \geq f_{\rm min}$). Since we choose $f_{\rm min} \gg g_{\rm min}$, the precise choice of $g_{\rm min}$ has negligible influence on the final spectra.

along the line-of-sight is $\sigma_l^2 = \sigma_r^2[1 - \beta(r)R^2/r^2]$, where R is the projected radius on the sky. The calculation of the observable projected kinematical quantities depends on whether one observes integrated light or individual stars. In the integrated light situation, the mean-squared projected line-of-sight velocity $\sigma_{\rm RMS}^2$ is the line-of-sight projection of $j\sigma_l^2$, divided by the line-of-sight projection of j. Here $j(r)$ is the three-dimensional luminosity density, which upon line-of-sight projection yields $I(R)$, the projected intensity. By contrast, for M15 we are in the discrete situation, which is generally more complicated. Instead of $j(r)$ one must know the three-dimensional number density of that population of stars from which the stars with kinematical measurements are drawn. This quantity is more difficult to estimate. To eliminate this complication we assume throughout our analysis that the number density of these stars is linearly proportional to the luminosity density $j(r)$, with a proportionality constant that is independent of position. So we assume that the average luminosity per observed star does not depend on position. This is a minor simplification, because it doesn't allow for gradients in the *visible* stellar population within the cluster. Note, however, that no assumption is made about the distribution of dark objects in the cluster, which is the much more important quantity for the dynamical predictions of the modeling.

In practice, we start the modeling from the V-band surface brightness profile $\mu_V(R)$ in mag/arcsec^2. For this we take the profile compiled from various sources by Trager et al. (1995). We correct this profile for $A_V = 0.28$ mag of extinction, which is based on the reddening $E(B-V) = 0.09$ (Harris 1996) and a standard Galactic reddening law with $A_V/E(B-V) = 3.1$ (Binney & Merrifield 1998). We transform this profile into a projected intensity $I(R)$ in $\mathrm{L}_\odot\,\mathrm{pc}^{-2}$. The Trager et al. profile is based exclusively on ground-based data. Because of this we do not use their profile inside of $R = 5''$, where it is compromised by seeing and crowding. For $R \le 5''$ we use the projected number density profile derived non-parametrically by Guhathakurta et al. (1996) from HST/WFPC2 data, scaled to match the Trager et al profile at $R = 5''$. This profile rises into the center of M15 approximately as a power law, $I(R) \propto R^{-0.82}$. Sosin & King (1997) inferred a slightly different profile from HST/FOC data, and they also found slightly different power-law slopes for different stellar masses. Inside $\sim 0.3''$ the number density profile is not well constrained by either study, due to the limited number of stars and uncertainties in the position of the M15 center. We have performed a variety of tests to assess the influence of these uncertainties on the predictions of our dynamical models. We have found that the main results are quite robust and do not depend sensitively on the exact choice of $I(R)$ in the central $5''$.

To calculate isotropic ($\beta = 0$) models for M15 we have used the non-parametric technique of Gebhardt & Fischer (1995). It solves an Abel integral to calculate $j(r)$ from $I(R)$. The mass density is then calculated as $\rho(r) = \Upsilon(r)j(r)$, where $\Upsilon(r)$ is an assumed mass-to-light ratio profile. Poisson's equation is then solved to obtain the gravitational potential $\Phi(r)$. To this we add the contribution $-GM_{\rm BH}/r$ of a possible central massive black hole. The Jeans equation (3) is then solved, and the results are projected along the line of sight to obtain $\sigma_{\rm RMS}(R)$. To calculate anisotropic models ($\beta \neq 0$), we have used the technique of van der Marel (1994). This technique starts with a parametric fit to $I(R)$, but otherwise proceeds similarly as the technique of Gebhardt & Fischer (1995). As a test, we used both techniques to calculate predictions for the case $\beta = 0$ and $\Upsilon(r) =$ constant, which yielded excellent agreement. In all model calculations we assumed a

distance to M15 of 10.0 kpc (Harris 1996).

5.2. Comparing the Data and Models

Data-model comparison can be performed qualitatively by visual comparison of a predicted profile $\sigma_{\rm RMS}(R)$ to the profile that was inferred from the data and is shown in Figure 9. However, quantitative data-model comparison is best performed using a maximum likelihood approach. We assume that the predicted velocity distribution at projected radius R is a Gaussian with dispersion $\sigma_{\rm RMS}(R)$. This is a reasonable assumption, at least for isotropic models (e.g., van der Marel & Franx 1993). Calculation of the full line-of-sight velocity distribution shape for spherical anisotropic models is not straightforward (e.g., Gerhard 1993; van der Marel et al. 2000) and is outside of the scope of the present paper (see Section 5.5 for a further discussion of anisotropic models). Let a star, number i, be observed at projected radius R_i. Let the uncertainty in its observed velocity v_i be Δv_i. The probability distribution $P_i(v)$ for the velocity v observed for star i is then a Gaussian with dispersion $[\sigma^2_{\rm RMS}(R_i) + \Delta v_i^2]^{1/2}$, centered on the cluster systemic velocity $v_{\rm sys}$. The total likelihood L of the dataset is the product of the quantities $P_i(v_i)$ for all of the $N = 1797$ stars in the combined velocity sample, so that

$$\lambda \equiv -2 \ln L = \sum_{i=1}^{N} \ln 2\pi[\sigma^2_{\rm RMS}(R_i) + \Delta v_i^2] + \sum_{i=1}^{N} (v_i - v_{\rm sys})^2 / [\sigma^2_{\rm RMS}(R_i) + \Delta v_i^2]. \qquad (4)$$

The models are generally characterized by a certain set of parameters. The parameters that yield the minimum λ value, $\lambda_{\rm min}$, are the ones that provide the best fit.

Once a best-fit model has been identified, there are two further questions that need to be answered: (a) is the best-fitting model statistically acceptable; and (b) what are the confidence regions around the best-fitting model parameters? To address the first question, we note that the last term in equation (4) is a χ^2 quantity. If each v_i is drawn from a Gaussian distribution with dispersion $[\sigma^2_{\rm RMS}(R_i) + \Delta v_i^2]^{1/2}$, which is what we assume here, then this term follows a χ^2 probability distribution with N degrees of freedom. For large N, this distribution has a mean N and dispersion $\sqrt{2N}$. So for the best-fit model to be statistically acceptable at the 1σ level, the value $\lambda_{\rm min}$ should be within $\pm\sqrt{2N}$ from the expectation value

$$\langle \lambda \rangle = \sum_{i=1}^{N} \ln 2\pi[\sigma^2_{\rm RMS}(R_i) + \Delta v_i^2] + N, \qquad (5)$$

where $\sigma_{\rm RMS}(R)$ is the profile predicted by the best-fit model. To address the second question, we use a well-known theorem of mathematical statistics (e.g., Stuart & Ord 1991; used also by Merritt & Saha 1993) which states that the likelihood-ratio statistic $\lambda - \lambda_{\rm min}$ tends to a χ^2 statistic in the limit of large N, with the number of degrees-of-freedom equal to the number of free parameters that have not yet been varied and chosen so as to optimize the fit. This is a consequence of the central limit theorem. Hence, the likelihood-ratio statistic $\lambda - \lambda_{\rm min}$ reduces to the well-known $\Delta\chi^2$ statistic (e.g., Press et al. 1992). This allows straightforward calculation of confidence regions around the best-fitting model parameters.

5.3. Isotropic Models with Constant Mass-to-Light Ratio

We started by calculating isotropic models with a (V-band) mass-to-light ratio Υ that is independent of radius. We allow for the possibility of a central black hole of mass $M_{\rm BH}$. Figure 11a shows the contours of the likelihood quantity λ in the $(\Upsilon, M_{\rm BH})$ plane. The solid contours show the 1, 2, 3, and 4σ confidence regions on the best-fitting model parameters. The best-fitting mass-to-light ratio is almost independent of $M_{\rm BH}$. This is because the black hole only influences the dynamical predictions close to the center, so that Υ is determined more-or-less uniquely by the data at large radii. By marginalizing over $M_{\rm BH}$, we infer a best-fitting mass-to-light ratio $\Upsilon = 1.6 \pm 0.1$. For understanding the dynamical structure of M15, the more interesting quantity is the black hole mass. By marginalizing over Υ we infer a best-fitting value $M_{\rm BH} = (3.2 \pm 2.2) \times 10^3\,{\rm M}_\odot$. The best-fitting model has likelihood $\lambda = 13405$. Equation (5) predicts that λ should be in the range 13419 ± 60, so the best-fit model is statistically acceptable.

Figure 11b compares the predicted and observed profiles of $\sigma_{\rm RMS}$ for fixed $\Upsilon = 1.6$ and different black hole masses. The model with $M_{\rm BH} = 0$ predicts a decrease in $\sigma_{\rm RMS}$ towards the center. This is a direct consequence of the fact that the luminosity and number density of M15 increase steeply towards the center (e.g., Tremaine et al. 1994). The observed $\sigma_{\rm RMS}$ profile does not show a decrease towards the center, requiring the presence of a central black hole for the models to fit the data.

As discussed in Section 1, there are independent constraints on the central mass distribution of M15 from observations of pulsar accelerations. The measured accelerations of two pulsars at $R = 1.1''$ from the cluster center yield a lower limit $M_{\rm cyl,min}(1.1'')$ on the M15 mass $M_{\rm cyl}(1.1'')$ enclosed within a cylinder of this radius. Equation (3.6) of Phinney (1993), combined with the pulsar data in his table 2, yields $M_{\rm min}(1.1'') = 4.5 \times 10^3\,{\rm M}_\odot$. The most likely (expectation) value for the enclosed mass, $\langle M_{\rm cyl}(1.1'')\rangle$, depends on the phase-space distribution of the pulsars in the cluster. Phinney (1993) quotes that for typical distributions $M_{\rm cyl,min}/\langle M_{\rm cyl}\rangle = 0.6$–$0.75$. This yields $\langle M_{\rm cyl}(1.1'')\rangle \approx (6.0$–$7.5) \times 10^3\,{\rm M}_\odot$. For the best fit model in Figure 11 we find that $M_{\rm cyl}(1.1'') = 6.3 \times 10^3\,{\rm M}_\odot$ (of which $3.2 \times 10^3\,{\rm M}_\odot$ in the form of a black hole, and $3.1 \times 10^3\,{\rm M}_\odot$ in the form of stellar objects). This is in excellent agreement with the pulsar constraints.

In our stellar dynamical analysis we have used the position of the cluster center given in Paper I, which is based on the analysis of Guhathakurta et al. (1996). This position has a 1-σ uncertainty of $0.2''$ in each coordinate, which corresponds to a two-dimensional 1-σ uncertainty of $0.3''$. This is small compared to the relevant scales in the analysis. For example, the kinematical profiles in Figure 9 only start at $R = 0.5''$ (this is the average radius of the innermost 11 data points, where 11 is the adopted data window size in `SROTATE`). More importantly, Figure 11b shows that models without a black hole fail to fit the data over the entire region $R \lesssim 6''$. Shifts in the assumed position of the M15 center of order $\sim 0.3''$ cannot change this. To quantify this, we repeated the likelihood analysis with several different assumed positions for the M15 center. These positions were obtained by shifting the nominal center position by $\sim 0.3''$ in various directions. The resulting changes in the best-fitting $M_{\rm BH}$ were found to be $\lesssim 0.1 \times 10^3\,{\rm M}_\odot$. This is much smaller than the formal error on $M_{\rm BH}$ ($2.2 \times 10^3\,{\rm M}_\odot$) and is therefore negligible. The same applies to the other models that are discussed in the remainder of this section. Hence, none of the main

results of the present study are affected by the uncertainties in the exact position of the M15 center.

5.4. Isotropic Models with Varying Mass-to-Light Ratio

The assumption of a mass-to-light ratio Υ that does not vary with radius is obviously a considerable simplification. M15 does not have a constant density core, which suggests that core-collapse has occurred as a result of two-body relaxation. A natural consequence of two-body relaxation is mass segregation. In an attempt to reach equipartition of energy, heavy stars and dark remnants sink to the center of the cluster, which causes a central increase in $\Upsilon(r)$. This boosts the predicted velocities close to the center, which may obviate the need to invoke a central black hole in the models (Peterson et al. 1989).

Detailed Fokker-Planck calculations are required to determine whether mass-segregation resulting from realistic initial conditions can fit the kinematical data for M15. We have not calculated such models ourselves. Instead, we have relied on the results published by Dull et al. (1997), which are the most recently published Fokker-Planck models for M15. The Dull et al. models were constructed to fit kinematical data at radii $R \gtrsim 4''$. It is therefore natural to ask how these models compare to the new data that is now available for $R \lesssim 4''$. Dull et al. do not show the kinematical predictions of their models inside $R = 3''$. However, they do show the run of $\Upsilon(r)$ in their best-fit model (their figure 12). We measured this profile from their paper, and used it as input into our Jeans models. We adopted the profile for the situation that is intermediate between a collapsed core and an expanded core, which provides the steepest central increase in Υ. We scaled $\Upsilon(r)$ uniformly downward by a factor 0.86, so as to best match the kinematical predictions shown by Dull et al. at radii $R \gtrsim 3''$. This scaling allows for differences in the adopted distance, foreground absorption, and surface brightness profile. The resulting mass-to-light ratio profile does not vary much at the radii $R \gtrsim 0.5''$ for which kinematical data is available, and is between 1.4 and 2.5 throughout. However, at smaller radii Υ increases to values $\gtrsim 10$, due to a central cusp that is strongly dominated by non-luminous neutron stars.

We constructed hydrostatic equilibrium models with the $\Upsilon(r)$ profile thus obtained from Dull et al.[7] and with a range of black hole masses. Figure 12b compares the predictions for $\sigma_{\rm RMS}$ to the observed profile from Figure 9d. Figure 12a shows the likelihood quantity λ as a function of $M_{\rm BH}$, together with the 1 and 2σ confidence levels. The best-fitting model has likelihood $\lambda = 13412$. Equation (5) predicts that λ should be in the range 13417 ± 60, so the best-fit model is statistically acceptable. The best-fitting black hole mass is $M_{\rm BH} = (4.5 \pm 2.1) \times 10^3\,{\rm M}_\odot$. So even with a realistic mass-to-light ratio profile $\Upsilon(r)$ inferred from Fokker-Planck models, the models still require a black hole to fit the data. The black hole mass is not very different from the value derived in Section 5.3 under the assumption of a constant Υ. The reason for this is that the enclosed mass inside a (three-dimensional) radius of $\sim 0.5''$ is only $\sim 1.0 \times 10^3\,{\rm M}_\odot$ larger for the

[7]Figure 12 of Dull et al. (1997) shows the mass-to-light ratio profile after projection along the line-of-sight, and not the intrinsic three-dimensional mass-to-light ratio profile. We properly accounted for this in our modeling.

Fokker-Planck models than it is for the constant Υ models. So even though in the former models there is a central concentration of dark remnants, the total mass in these remnants is insufficient to explain the observed kinematics. In fact, with the $\Upsilon(r)$ profile from Dull et al. (1997), the models require a larger BH mass than for a constant Υ (namely, $[4.5 \pm 2.1] \times 10^3\,\mathrm{M}_\odot$ versus $[3.2 \pm 2.2] \times 10^3\,\mathrm{M}_\odot$). This is because $\Upsilon(r)$ actually decreases radially inwards between ~ 1 arcmin and $\sim 3''$ (presumably caused by mass segregation concentrating the giants in the center compared to less massive stars). The best-fit model in Figure 12 has a mass $M_{\rm cyl}(1.1'') = 9.1 \times 10^3\,\mathrm{M}_\odot$ within a cylinder of radius $R = 1.1''$ (of which $4.5 \times 10^3\,\mathrm{M}_\odot$ in the form of a black hole, and $4.6 \times 10^3\,\mathrm{M}_\odot$ in the form of stellar objects). This is somewhat larger than the expectation value implied by the pulsar constraints, $\langle M_{\rm cyl}(1.1'')\rangle \approx (6.0\text{–}7.5) \times 10^3\,\mathrm{M}_\odot$ (Section 5.3), but the residual is not statistically unacceptable.

A large uncertainty in Fokker-Planck models comes from the assumptions used for the retention factor of neutron stars. Dull et al. (1997) assume that all neutron stars are retained. However, the distribution of pulsar kick velocities suggests that most of the neutron stars (assuming that all pulsars come from neutron stars) should have been ejected from the cluster due to the low escape velocity of M15. The best estimates for the retention factor are generally around a few percent and never go above 10% (Drukier 1996; Davies & Hansen 1998; Pfahl, Rappaport & Podsiadlowski 2002). Even more extreme, Hansen & Phinney (1997) suggest less than 1% of single neutron stars would be retained. Binaries, however, provide a mechanism in which the neutron star retention factor may be increased, but, even when assuming a large binary fraction, the retention factor is still below 10% (Davies & Hansen 1998; Pfahl, Rappaport & Podsiadlowski 2002). Thus, it appears that the contribution from neutron stars may not be very significant for the central mass distribution in globular clusters. Heavy white dwarfs (1–1.3 $\mathrm{M}_\odot$) do not suffer from these large birth kicks and so can provide some contribution to the central mass, but these objects are not as centrally-concentrated (Dull et al. 1997). The best way to understand the effect of stellar remnants is to include evolutionary models with realistic assumptions for the retention factor. The important conclusion in the present context is that the Dull et al. models strongly overestimate the expected neutron star retention, yet still fail to fit the M15 data without a central black hole.

The number of stars that end up as neutron stars or white dwarfs in Fokker-Planck models depends critically on the assumed initial mass function (IMF). The more stars there are at the high end of the IMF, the higher the predicted central velocity dispersion at the present epoch (e.g., Grabhorn et al. 1992). However, there are good observational constraints on the present-day local mass function (MF) of M15, at least below the main-sequence turn-off ($\sim 0.7\,\mathrm{M}_\odot$ for M15). The IMF can therefore not be treated as a completely free parameter. The MF obtained from HST photometry by De Marchi & Paresce (1995) for a field at $R = 4.6$ arcmin from the M15 center has a power-law slope $x \approx 1.3$ at masses above $\sim 0.25\,\mathrm{M}_\odot$ (where x is defined so that a Salpeter MF has $x = 1.35$). Dull et al. (1997) use a global IMF slope $x = 0.9$ at these masses, which yields a local present-day MF slope $x \approx 1.2$ at $R = 4.6$ arcmin (figure 8 of Grabhorn et al. 1992). This indicates that the Dull et al. IMF is approximately correct, and if anything, is slightly too shallow. So there is little room for an increased number of high mass stars in the IMF, which would be needed to bring the Dull et al. models in better agreement with the kinematical

data presented here. One would actually like the Fokker-Planck models to reproduce also the observational constraints on the radial dependence of the present-day MF (De Marchi & Paresce 1995; Sosin & King 1997). A preliminary report of attempts at this (Murphy et al. 1997) indicates that such models predict a present-day total number of ~ 7000 non-luminous $1.4\,M_\odot$ objects in M15. This is 30% less than the number of such objects in the Dull et al. models. Hence, more accurate modeling of the IMF is not likely to improve the fit to the kinematical data presented here.

The Fokker-Planck models of Dull et al. (1997) are the most recent ones to have been constructed for M15, but they are not the only ones. The Dull et al. models built on previous work by Grabhorn et al. (1992). Both papers used the same Fokker-Planck methodology and adopted the same IMF for their best fit. The main difference is that Dull et al. had access to more modern and extensive data to compare their models to. The models of Dull et al. therefore supersede the models of Grabhorn et al. Also, the discussion that was presented above with respect to the Dull et al. models applies equally to the models of Grabhorn et al. In another study, Phinney (1993) fitted an independent set of Fokker-Planck models to M15 data. These models were calculated by Bryan Murphy using an extension of the code described by Murphy, Cohn & Hut (1990). These models had several nice features, including explicit inclusion of stellar evolution and neutron-star escape. However, the models used a pure power-law IMF. This is less accurate than the IMF used by Grabhorn et al. and Dull et al. and is not consistent with our current understanding of globular cluster IMFs (e.g., Paresce & De Marchi 2000). As mentioned above, a model cannot be considered to be acceptable unless it fits observational constraints on the present-day MF. Also, Phinney's model that comes closest to fitting the presently available kinematical data for M15 (his model z120) must be evolved for 21.4 Gyr. This considerably exceeds the accepted age of the Universe (e.g., Lineweaver 1999).

The above arguments indicate that there is an urgent need for more detailed Fokker-Planck modeling of the structure and evolution of M15. The models should include as much as possible of the relevant physics, including neutron star escape. The most current datasets must be used to constrain the cluster density, kinematics and IMF. With such a study it will be possible to explore in much more detail than has been possible here whether the observed kinematics of M15, both the central $\sigma_{\rm RMS}$ and its dependence on radius, can be explained without requiring a central black hole.

5.5. Anisotropic Models

To further explore the range of models that can reproduce the observed kinematical profiles for M15 we have also constructed models with an anisotropic velocity distribution. Models with radial velocity dispersion anisotropy predict a larger projected velocity dispersion near the center of a stellar system than models with an isotropic velocity dispersion (e.g., Binney & Mamon 1982). Radially anisotropic models for M15 may therefore be able to fit the data without invoking a central black hole. To test how much radial anisotropy is required for this, we constructed models

in which the anisotropy function $\beta \equiv 1 - \sigma_t^2/\sigma_r^2$ is parameterized as

$$\beta(r) = \beta_0 + (\beta_\infty - \beta_0)\frac{r^2}{r^2 + a^2}. \quad (6)$$

This parameterization yields a convenient semi-analytical expression for the solution of the Jeans equation (van der Marel 1994). It corresponds to a profile that varies from $\beta = \beta_0$ at the center to $\beta = \beta_\infty$ at large radii. The transition occurs at the scale radius a.

The value of β_∞ has little influence on the dynamical predictions near the center of the cluster, which is where isotropic models without a central black hole fail to fit the data (cf. Figure 11). Without loss of generality we therefore kept β_∞ fixed at zero in our study. We also assumed that the mass-to-light ratio Υ is constant as a function of radius, and we did not include a black hole (i.e., $M_{\rm BH} = 0$). This leaves three free parameters, β_0, a and Υ, which were varied to optimize the fit to the data. The best-fitting model was found to have $\beta_0 = 0.65$, $a = 18''$ and $\Upsilon = 1.6$. The inferred mass-to-light ratio is similar to that inferred for isotropic models (Section 5.3). The best-fitting model has likelihood $\lambda = 13401$. Equation (5) predicts that λ should be in the range 13395 ± 60, so the model is statistically acceptable. Figure 13b compares the predictions for the best-fitting anisotropic model (dotted curve) to the observed $\sigma_{\rm RMS}$ from Figure 9d. For comparison, we also show the predictions for models in which β_0 was kept fixed at $\beta_0 = 0$, 0.2, 0.4 and 0.8, and in which only a and Υ were varied to optimize the fit. Figure 13a shows the likelihood quantity λ for these fits as a function of β_0, together with the 1 and 2σ confidence levels. The best fit and its 1σ error are $\beta_0 = 0.65 \pm 0.2$.

The models in Figure 13 show that it is possible to fit the M15 data without invoking a central mass concentration. However, this requires that $\sigma_r = 1.6\sigma_t$ (i.e., $\beta \approx 0.65$) throughout much of the central region of M15. Such a high value is difficult to reconcile with our current understanding of the dynamical structure of globular clusters. Even elliptical galaxies, which are collisionless, do not have such large anisotropies (e.g., Kronawitter et al. 2000). By contrast, in a cluster like M15 considerable two-body relaxation must have occurred near the center, which tends to isotropize the velocity distribution (Peterson et al. 1989). This has been demonstrated explicitly, both with anisotropic Fokker-Planck calculations in energy–angular momentum space and with N-body calculations (Takahashi 1996; Baumgardt, Heggie & Hut 2002). In the region that contains the central $\sim 20\%$ of the cluster mass, the anisotropy parameter β remains between 0 and 0.1 at all times during the cluster evolution. Larger radial anisotropies can develop in the outskirts of the cluster, but we verified explicitly that this does not change the interpretation of the central kinematics of M15.

6. Discussion and Conclusions

We have obtained high spatial resolution spectroscopy of the central region of the globular cluster M15 with the STIS spectrograph on board HST. The observational setup, calibration and spectral extraction were discussed in Paper I. Here we have analyzed the spectra with a cross-correlation technique to determine the line-of-sight velocities of individual stars. Our final

STIS velocity sample contains 64 stars. Two-thirds of the stars in this sample have their velocity measured for the first time. Half of the stars reside within a projected radius $R = 2.4''$ from the center of M15. The new data set triples the number of stars with measured velocities in the central $R \leq 1''$ of M15 and doubles the number in the central $R \leq 2''$. Our analysis includes the necessary (small) corrections for the effects of blending with neighboring stars. Detailed tests on a calibration star and comparison to ground-based M15 data demonstrate that our velocities are accurate and trustworthy. We combined the STIS results with existing ground-based data to obtain a total sample of 1797 stars in M15 with known line-of-sight velocities. We use the combined sample to determine the radial profiles of the most important projected kinematical quantities: the rotation velocity $V_{\rm rot}$; the position angle of the kinematical major axis, $\mathrm{PA_{kin}}$; the velocity dispersion, σ; and the RMS velocity averaged over rings on the projected plane of the sky, $\sigma_{\rm RMS}$. Our results differ from earlier work only in the central few arcsec. In particular, we find that $\sigma_{\rm RMS}$ rises to $\sim 14\,\mathrm{km\,s^{-1}}$ at the innermost radii. This is somewhat higher than the value of 10–$12\,\mathrm{km\,s^{-1}}$ inferred previously from ground-based data (Dull et al. 1997; Gebhardt et al. 2000a).

To interpret the results we constructed dynamical models based on the Jeans equation for a spherical system. We compared the model predictions to the data using a maximum-likelihood technique to obtain the best-fitting model parameters and their confidence regions. If the velocity distribution is isotropic, then M15 must have a central concentration of non-luminous material. This could be due to an intermediate-mass black hole. If one were reluctant to invoke such an object, then one alternative may be that M15 has a central collection of dark remnants (neutron stars and/or stellar mass black holes). This arises naturally in a globular cluster due to the mass segregation that occurs as two-body relaxation drives the system to equipartition. However, we argued that the best-fitting Fokker-Planck models that have previously been constructed for M15 (Dull et al. 1997) do not predict a large enough concentration of dark remnants to fit the data. It remains to be seen whether alternative Fokker-Planck models can be constructed that generate a more massive concentration of dark remnants from plausible initial conditions. It is useful to note in this context that an important uncertainty in Fokker-Planck models comes from the assumptions used for the retention factor of neutron stars. Dull et al. assumed that all neutron stars are retained, in contrast with most recent work which predicts that only $\lesssim 10\%$ will be retained. So Dull et al. may actually have overestimated the central concentration of dark remnants in their models. Another alternative scenario is to assume that deviations from isotropy in the velocity distribution may be responsible for the observed kinematics. However, to fit the kinematical data without any mass concentration one must assume that the velocity distribution is radially anisotropic near the center, $\beta_0 = 0.65 \pm 0.2$. This contradicts the predictions of both Fokker-Planck models and N-body calculations, which suggest that the velocity distribution in the central region of a globular clusters remains close to isotropic at all times during the cluster evolution.

In view of the results that we have presented, the presence of an intermediate mass black hole in M15 appears to be the most plausible explanation of the data. As noted in Section 1, there are several mechanisms by which such a black hole could plausibly have formed. For the best-fit black hole mass we adopt the average of the values which were inferred in Sections 5.3 and 5.4 using a constant mass-to-light ratio and the Dull et al. (1997) mass-to-light ratio profile,

respectively. This yields: $M_{\rm BH} = (3.9 \pm 2.2) \times 10^3 \, {\rm M}_\odot$. This mass is consistent with the constraints on the central mass distribution of M15 implied by observations of pulsar accelerations (Phinney 1993). The black hole mass inferred for M15 matches remarkably well with the understanding that has been developed for the presence of black holes in the centers of galaxies. For these black holes, there is a strong correlation between the black hole mass and the velocity dispersion of the bulge component (Gebhardt et al. 2000b; Ferrarese & Merritt 2000). Figure 14 shows the available data points and the best fit from the recent compilation of Tremaine et al. (2002). For M15, the luminosity weighted mean velocity dispersion within the half light radius (1.06 arcmin, Harris 1996) is $12.1 \, {\rm km \, s^{-1}}$ (this quantity was defined and calculated similarly as in Gebhardt et al. 2000b). At this dispersion, the estimated black hole mass fits perfectly on the extrapolation of the relation established for galaxies (Figure 14). Interestingly, a study of the globular cluster G1 in the Andromeda galaxy, performed simultaneously with the present study, has also provided evidence for a central black hole (Gebhardt, Rich & Ho 2002). Like M15, this globular cluster fits perfectly on the relation shown in Figure 14. This independent research strengthens the interpretation of the M15 data in terms of an intermediate-mass black hole. It has generally been believed that globular clusters and galaxies form and evolve quite differently, so it could be that it is a mere coincidence that they fall on the same $M_{\rm bh}$—σ relationship. However, it could also have some deep physical significance. For example, it may point to a new link between galaxy formation and globular cluster formation. Or it may point to a link between the black holes in these systems. For example, it could be that the massive black holes in galaxies grew from seed black holes that arose in clusters. There may also be a link with the intermediate luminosity X-ray objects that are known to exist in external galaxies, and which have been argued to be intermediate mass black holes. These issues will need to be explored with future observational and theoretical studies.

Despite the interesting evidence for the presence of an intermediate mass black hole in M15, some words of caution are justified. All of the dynamical models that have been constructed for M15 remain somewhat idealized. This is true both for the Jeans models presented here and for the Fokker-Planck models presented elsewhere. For example, the Jeans models assume exact hydrostatic equilibrium, which is generally expected to be a good assumption (see Section 5.1). Nonetheless, during periods of particularly rapid evolution in the cluster structure this assumption could yield results that are biased. Fokker-Planck models can address the cluster evolution directly and do not need to rely on the assumption of hydrostatic equilibrium. On the other hand, the results of Fokker-Planck models depend strongly on the processes of stellar evolution and binary heating, both of which are generally modeled only in rudimentary ways. More generally, globular clusters are complicated systems from a theoretical viewpoint, much more so than galaxies, and not all of the essential physics may yet have been fully understood. There is some evidence from observations that this may indeed be the case. For example, M15 rotates quite rapidly in the central regions (cf. Figure 9), and this is not naturally explained by any theoretical model (Gebhardt et al. 2000a). Also, the $\sigma_{\rm RMS}$ of M15 appears to have a small dip at intermediate radii (at $R \approx 13''$), which is not naturally explained by any of the models constructed here (Figures 11–13). Further studies to test the observational reality of these features would be valuable, as would further theoretical work to address their origin.

We have assumed throughout our study, as has previous work on M15, that the observed

kinematics are characteristic of the cluster, and are not contaminated by possible orbital motion of stars in binary systems. There are several reasons that make this a reasonable assumption (Hut et al. 1992). The binary fraction of globular clusters is believed to be only of order 10%. Also, most of the stars in the velocity sample are red giants. Their relatively large radii imply that any binaries must have large separations and orbital velocities $\lesssim 25\,\mathrm{km\,s^{-1}}$. Inclination, phase and ellipticity effects imply that for an average binary at a random epoch only a fraction of the velocity amplitude will be observed along the line of sight. These issues conspire to make it extremely challenging to identify even a few binaries in globular clusters from large line-of-sight velocity studies, even with high quality multi-epoch data (Pryor et al. 1989). One can turn this around to argue that the average observed kinematics of large samples of stars should not be influenced significantly by any orbital motion in binaries. This assumption is supported by the fact that the mass distribution inferred here from stellar kinematics agrees with that inferred from pulsar studies. Nonetheless, it would be useful for future studies to attempt a detailed quantitative assessment of the potential contamination of the line-of-sight kinematics of globular clusters by binaries.

In the future it may be possible to strengthen the observational constraints on the central structure of M15 through proper motion studies. With two additional velocity components it will be possible to directly establish the (an)isotropy of the stellar velocity distribution. It has been demonstrated that such studies are feasible with HST (e.g., Anderson & King 2000). However, the severe crowding in the central few arcsec of M15 may provide a significant hurdle to overcome. An alternative way to strengthen the observational constraints would be to increase the sample of radial velocities. This would require inclusion of fainter stars near the turnoff magnitude ($V \approx 19$ in M15), which were inaccessible to our STIS study because of limited S/N. In principle, a 4m class telescope has sufficient light gathering power to perform such a study in a reasonable amount of time. By centering the spectra around the CO band-head (2.3μm), it may be possible to take full advantage of adaptive optics to attain a spatial resolution comparable to that of HST.

Support for proposals #8262 was provided by NASA through a grant from the Space Telescope Science Institute, which is operated by the Association of Universities for Research in Astronomy, Inc., under NASA contract NAS 5-26555. We thank Pierre Dubath for helpful advice in the early stages of this project. We thank the anonymous referee for useful feedback that helped improve the presentation of the paper.

REFERENCES

Anderson, J., & King, I. R. 2000, PASP, 112, 1360

Bahcall, J. N., & Wolf R. A. 1976, ApJ, 209, 214

Bahcall, J. N., & Wolf R. A. 1977, ApJ, 216, 883

Baumgardt, H., Heggie, D. C., & Hut, P. 2002, MNRAS, in press [astro-ph/0206258]

Binney, J. J., & Mamon G. A. 1982, MNRAS, 200, 361

Binney, J. J., & Merrifield, M. 1998, Galactic Astronomy (Princeton: Princeton University Press)

Binney, J., & Tremaine, S. 1987, Galactic Dynamics (Princeton: Princeton University Press)

Colbert, E. J. M., & Mushotzky, R. F. 1999, ApJ, 519, 89

d'Amico, N., Possenti, A., Fici, L., Manchester, R. N., Lyne, A. G., Camilo, F., & Sarkissian, J. 2002, ApJL, 570, L89

Davies, M., & Hansen, B. 1998, MNRAS, 301, 15

De Marchi, G., & Paresce, F. 1995, A&A, 304, 202

Djorgovski, S., & King, I. 1986, ApJ, 305, 61

Drukier, G. A. 1996, MNRAS, 280, 498

Drukier, G. A., Slavin, S. D., Cohn, H. N., Lugger, P. M., Berrington, R.C., Murphy, B. W., & Seitzer, P. O. 1998, AJ, 115, 708

Dubath, P., Meylan, G., & Mayor, M. 1994, ApJ, 426, 192

Dull, J. D., Cohn, H. N., Lugger, P. M., Murphy, B. W., Seitzer, P. O., Callanan, P. J., Rutten, R. G. M., & Charles, P. A. 1997, ApJ, 481, 267

Ferrarese, L., & Merritt, D. 2000, ApJ, 539, L9

Gebhardt, K., Pryor, C., Williams, T. B., & Hesser, J. E. 1994, AJ, 107, 2067

Gebhardt, K., & Fischer, P. 1995, AJ, 109, 209

Gebhardt, K., Pryor, C., O'Connell, R. D., Williams, T. B., & Hesser, J. E. 2000a, AJ, 119, 1268

Gebhardt, K., et al. 2000b, ApJ, 539, L13

Gebhardt, K., Rich, R. M., & Ho, L. 2002, ApJL, in press

Gerhard, O. E. 1993, MNRAS, 265, 213

Grabhorn, R. P., Cohn, H. N., Lugger, P. M., & Murphy, B. W. 1992, ApJ, 392, 86

Guhathakurta, P., Yanny, B., Schneider, D. P., & Bahcall, J. N., 1996, AJ, 111, 267

Hansen, B., & Phinney, E. S. 1997, MNRAS, 291, 569

Harris, W.E. 1996, AJ, 112, 1487

Hut, P., et al. 1992, PASP, 104, 981

Kormendy, J., & Gebhardt, K. 2001, in 'Proc. 20th Texas Symposium on relativistic astrophysics', AIP conference proceedings, Vol. 586., eds., J. C. Wheeler, & H. Martel, p. 363 (NY: American Institute of Physics)

Kronawitter, A., Saglia, R. P., Gerhard, O., Bender, R. 2000, A&AS, 144, 53

Kurtz, M. J., & Mink, D. J. 1998, PASP, 110, 934

Lauer, T. R., et al. 1991, ApJ, 369, L45

Lee, H. M. 1987, ApJ, 319, 801

Lee, M. H. 1993, ApJ, 418, 147

Lee, H. M. 1995, MNRAS, 272, 605

Lineweaver, C. 1999, Science, 284, 1503

Lugger, P. M., Cohn, H., Grindlay, J. E., Bailyn, C. D., Hertz, P. 1987, ApJ, 320, 482

Mayor, M. 1980, A&A, 87, L1

Merritt, D. R., & Saha, P. 1993, ApJ, 409, 75

Miller, M. C., & Hamilton, D. P. 2002, MNRAS, 330, 232

Mouri, H., & Taniguchi, Y. 2002, ApJ, 566, L17

Murphy, B. W., Cohn, H. N., & Hut, P. 1990, MNRAS, 245, 335

Murphy, B. W., Cohn, H. N., Lugger, P. M., & Drukier, G. A. 1997, BAAS, 29, 1338

Paresce, F., & De Marchi, G. 2000, ApJ, 534, 870

Peterson, R. C. 1993, in Structure and Dynamics of Globular Clusters, eds., G. Djorgovski & G. Meylan, ASP Conference Series, Vol. 50, p. 65

Peterson, R. C., Seitzer, P., & Cudworth, K. M. 1989, ApJ, 347, 251

Pfahl, E., Rappaport, S., & Podsiadlowski, P. 2002, ApJ, 573, 283

Phinney, E. S. 1993, in Structure and Dynamics of Globular Clusters, eds., G. Djorgovski & G. Meylan, ASP Conference Series, Vol. 50, p. 141

Portegies Zwart, S. F., & McMillan, S. L. W. 2002, ApJ, in press [astro-ph/0201055]

Press, W. H., Teukolsky, S. A., Vetterling, W. T., & Flannery, B. P. 1992, Numerical Recipes (Cambridge: Cambridge University Press)

Pryor, C., McClure, R. D., Fletcher, J. M., & Hesser, J. E. 1989, in Dynamics of Dense Stellar Systems, ed. D. Merritt, p. 175 (Cambridge: Cambridge University Press)

Quinlan, G. D., & Shapiro, S. L. 1987, ApJ, 321, 199

Quinlan, G. D., & Shapiro, S. L. 1990, ApJ, 356, 483

Rees, M. J. 1984, ARA&A, 22, 471

Sanders, R. H. 1970, ApJ, 162, 791

Smith, H. A. 1995, RR Lyrae Stars (Cambridge: Cambridge University Press)

Sneden, C., & Parthasarathy, M. 1983, ApJ, 267, 757

Sosin, C., & King, I. R. 1997, AJ, 113, 1328

Stuart, A., & Ord, J. K. 1991, Kendall's Advanced Theory of Statistics, Volume II, 5th ed. (London: Edward Arnold, a division of Hodder & Stoughton)

Takahashi, K. 1996, PASJ, 48, 691

Tonry, J., & Davis, M. 1979, AJ, 84, 1511

Trager, S. C., King, I. R., & Djorgovski, S. 1995, AJ, 109, 218

Tremaine, S., Richstone, D. O., Byun, Y.-I., Dressler, A., Faber, S. M., Grillmair, C., Kormendy, J., Lauer, T. R. 1994, AJ, 107, 634

Tremaine, S., et al. 2002, ApJ, 574, 740

van der Marel, R. P. 1994, MNRAS, 270, 271

van der Marel, R. P. 2001, in 'Black Holes in Binaries and Galactic Nuclei', Kaper L., van den Heuvel E. P. J., Woudt P. A., eds., Springer-Verlag, p. 246

van der Marel, R. P., & Franx, M. 1993, ApJ, 407, 525

van der Marel, R. P., Gerssen, J., Guhathakurta, P., Peterson, R. C., & Gebhardt, K. 2002, AJ, in press (Paper I)

van der Marel R.P., Magorrian J., Carlberg R.G., Yee H.K.C., Ellingson E. 2000, AJ, 119, 2038

Zaggia, S., Capaccioli, M., & Piotto, G. 1993, A&A, 278, 415

Zezas, A., & Fabbiano, G. 2002, ApJ, submitted [astro-ph/0203176]

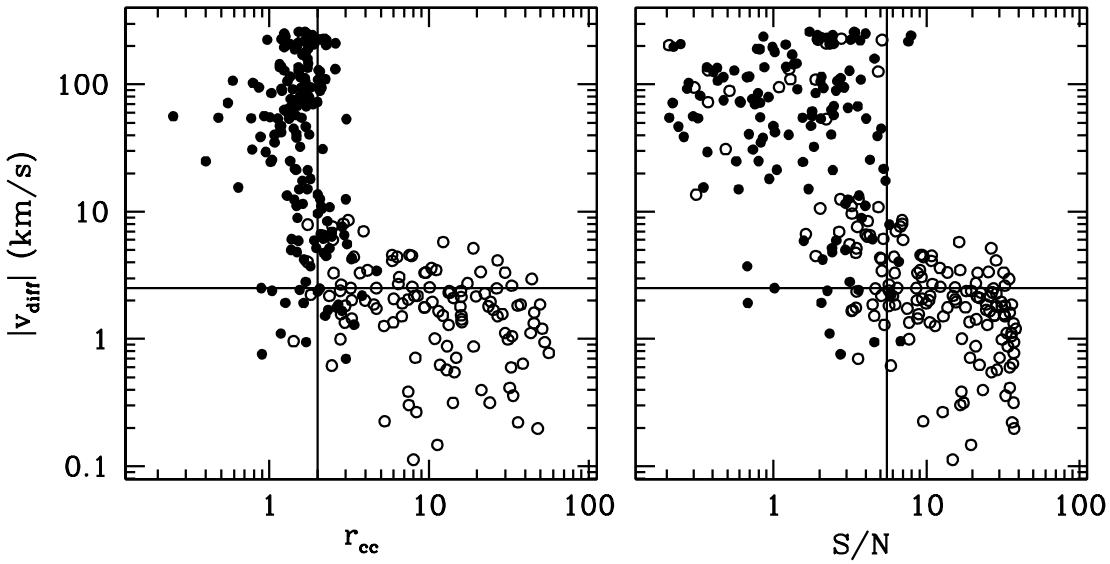

Fig. 1.— Radial velocity determination tests for 294 HST/STIS spectra of the calibration star. **(a; left panel)** Absolute difference $|v_{\rm diff}|$ (in $\mathrm{km\,s^{-1}}$) between the measured radial velocity and true calibration star velocity as a function of the cross-correlation statistic $r_{\rm cc}$. Open symbols indicate spectra with average signal-to-noise ratio $S/N \geq 5.5$ per pixel and closed symbols indicate spectra with $S/N < 5.5$. The vertical line indicates the cutoff $r_{\rm cc} = 2$ that we have used in the analysis. **(b; right panel)** Absolute difference $|v_{\rm diff}|$ (in $\mathrm{km\,s^{-1}}$) between the measured radial velocity and true calibration star velocity as a function of S/N. Open symbols indicate spectra with $r_{\rm cc} \geq 2$ and closed symbols indicate spectra with $r_{\rm cc} < 2$. The vertical line indicates the cutoff $S/N = 5.5$ that we have used in the analysis. Both panels show a pronounced transition from unreliable measurements to reliable measurements, either with increasing $r_{\rm cc}$ or with increasing S/N. Spectra that have both $r_{\rm cc} \geq 2$ and $S/N \geq 5.5$ (the open symbols to the right of the cut-off line in each panel) yield a reliable measurement of the stellar velocity. The horizontal line in both panels corresponds to $2.5\,\mathrm{km\,s^{-1}}$, which is the systematic uncertainty in the velocity calibration of the data (cf. Paper I). The axes in both panels are logarithmic.

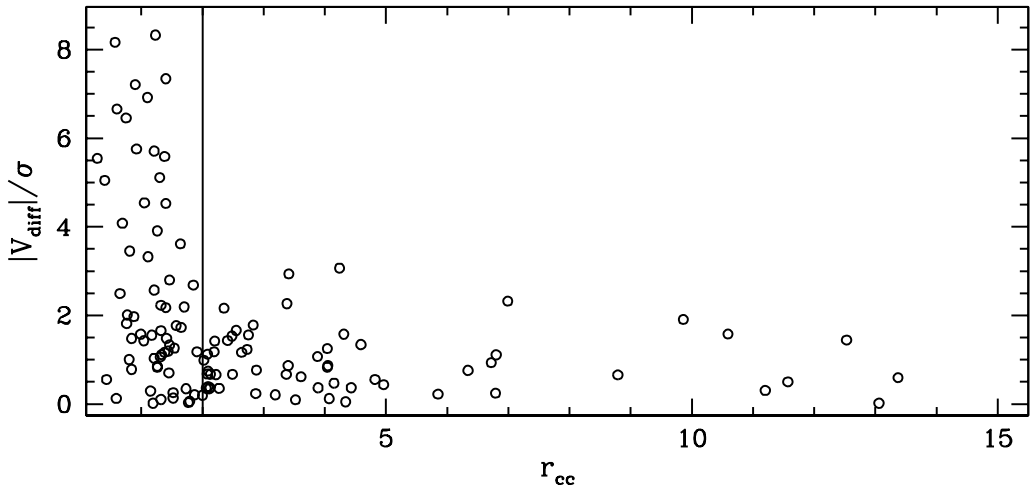

Fig. 2.— Cross-correlation results for HST/STIS spectra of M15 stars. Spectra with an average signal-to-noise ratio $S/N \geq 5.5$ per pixel were extracted for 131 stars. The ordinate of the figure shows the absolute difference $|v_{\rm diff}|$ of the inferred stellar velocity and the systemic velocity of M15, divided by the central velocity dispersion of M15 (assumed to be $12\,{\rm km\,s^{-1}}$, Gebhardt et al. 2000). This 'normalized velocity deviation' is shown as function of cross-correlation statistic $r_{\rm cc}$. A large value of the normalized velocity deviation generally indicates that the inferred stellar velocity is incorrect. There is a pronounced transition from unreliable measurements to reliable measurements with increasing $r_{\rm cc}$. The cutoff at $r_{\rm cc} = 2$ that we have used in our analysis (vertical line) excludes all measurements that are obviously unreliable. This confirms the analysis of the calibration star spectra presented in Figure 1.

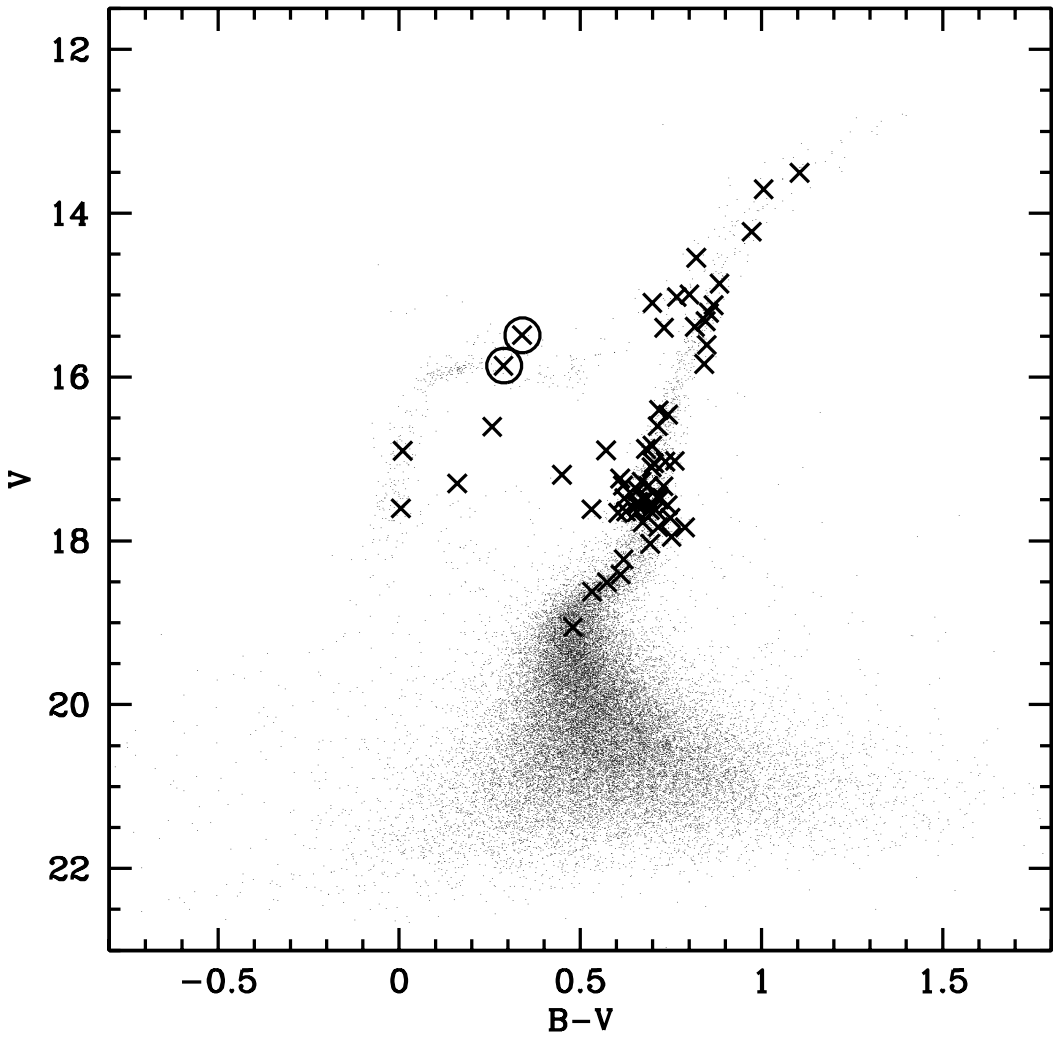

Fig. 3.— Color-magnitude diagram of the stars in M15, obtained from the photometric HST/WFPC2 imaging catalog presented in Paper I. The crosses indicate the location of the stars for which we have derived reliable radial velocities from the HST/STIS spectra. The two encircled crosses indicate potential RR Lyrae variables which were not included in the dynamical modeling.

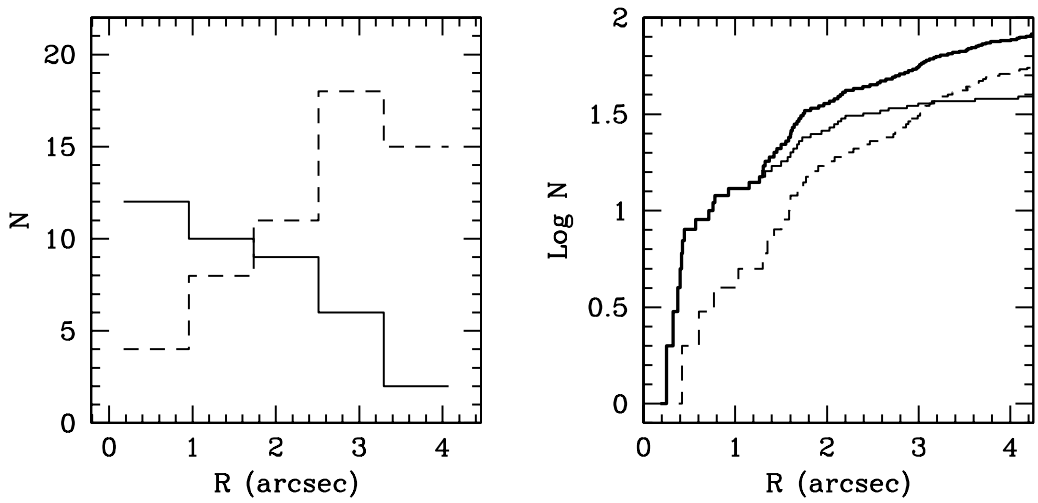

Fig. 4.— Distribution of the number of M15 stars N with known line-of-sight velocities (with errors $\leq$ 10 $\mathrm{km\,s^{-1}}$) as function of projected radius from the cluster center. **(a; left panel)** Binned histogram. Solid line: the HST/STIS velocity sample; Dashed line: the sample with ground-based measurements compiled by Gebhardt et al. (2000a). **(b; right panel)** Logarithm of the cumulative distribution (i.e., total number of stars within a given radius). Solid line: the HST/STIS velocity sample; Dashed line: the Gebhardt et al. (2000a) compilation; Heavy solid line: the combined HST/STIS and ground-based sample, corrected for double entries (i.e., stars present in both samples are counted only once). The HST/STIS data significantly increase the number of stars with known line-of-sight velocities close to the cluster center.

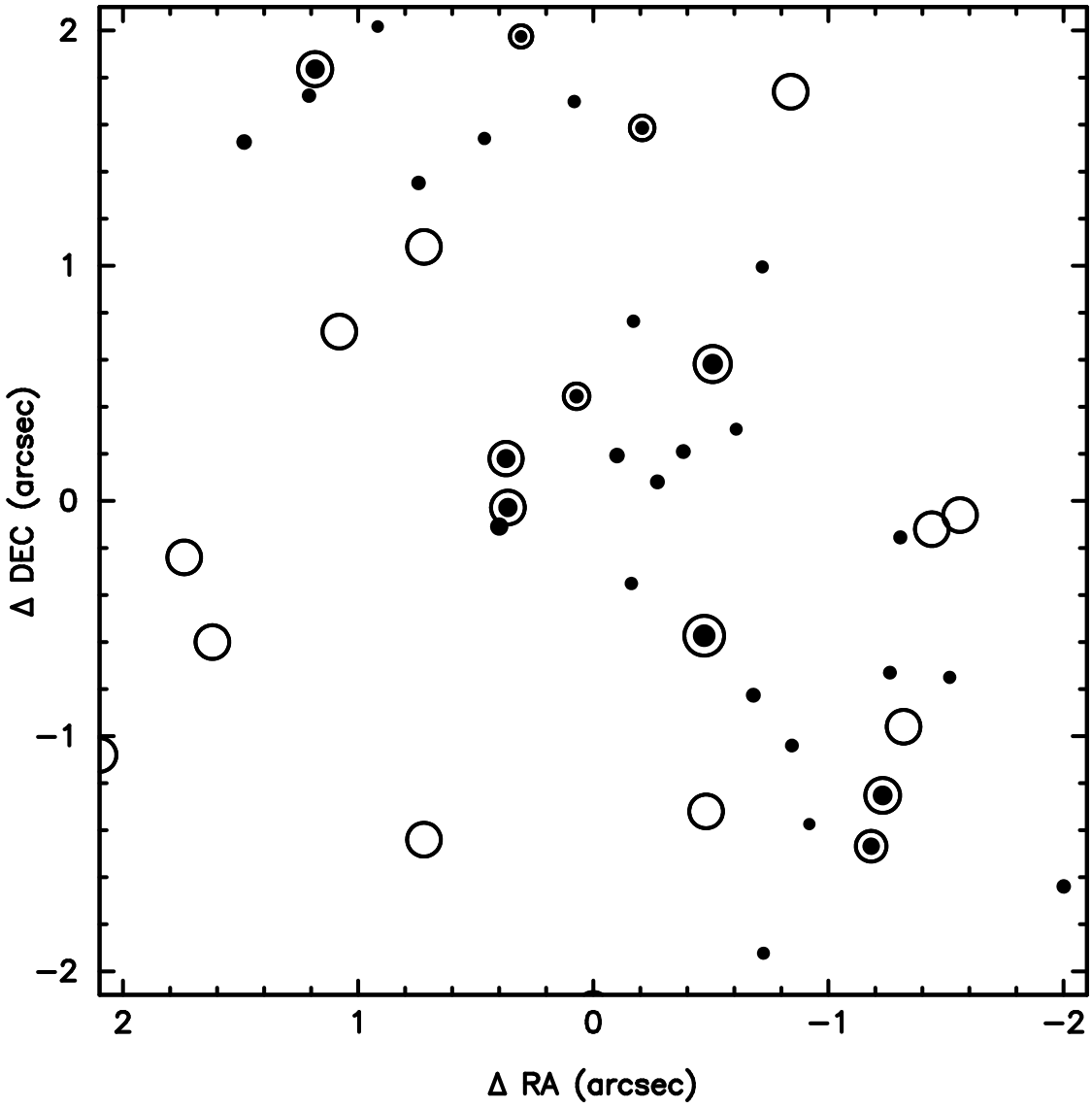

Fig. 5.— Positions of the stars with known line-of-sight velocities in the central 4×4 arcsec of M15. Coordinates are (RA, DEC) with respect to the cluster center determined by Guhathakurta et al. (1996). Filled dots: stars with a velocity measurement from STIS; Circles: stars with a ground-based velocity measurement. The symbol size provides a measure of the brightness of the star; the circles were increased in size relative to the filled dots to avoid overlapping symbols. The STIS measurements cluster around a line with a position angle of 26.65°, which was the slit position angle used for the observations (see Paper I).

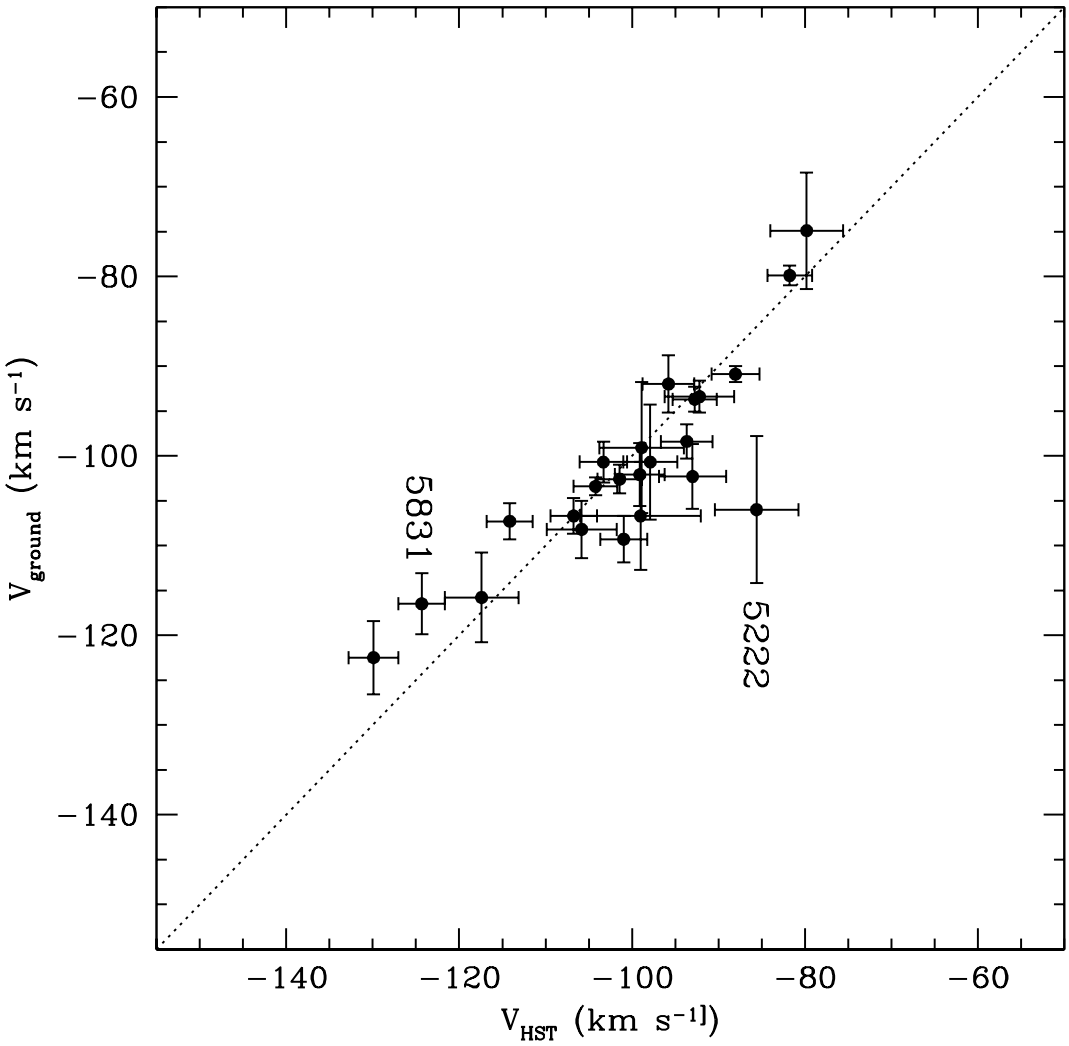

Fig. 6.— Comparison of the velocities derived with HST/STIS to those obtained from ground-based data, for those stars for which both exist. The excellent agreement shows that there are no unidentified systematic errors in the data. The two labeled stars are discussed in the text.

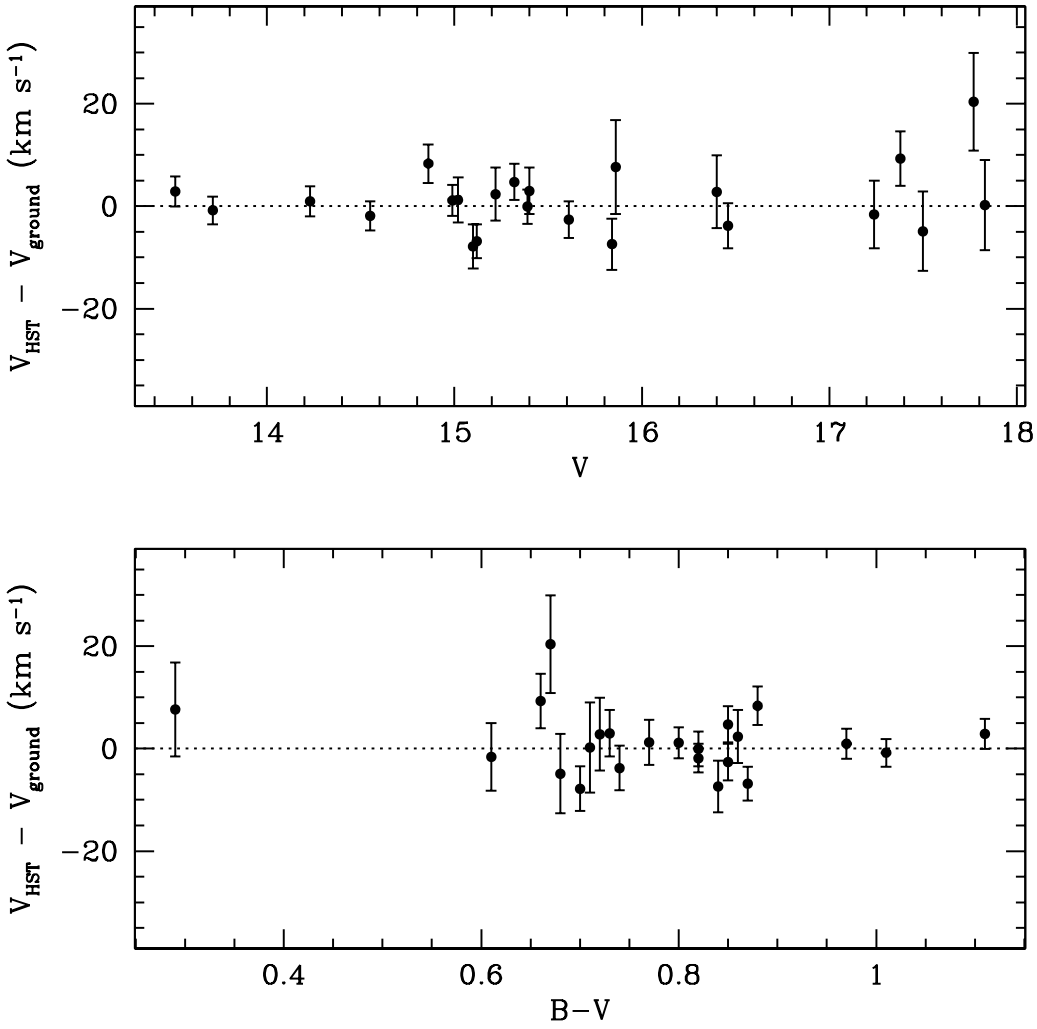

Fig. 7.— Velocity residuals, $v_{\rm HST} - v_{\rm ground}$, for those stars that have both HST/STIS and ground-based measurements of their line-of-sight velocities. **(a; top panel)** Residuals as a function of stellar magnitude V. **(b; bottom panel)** Residuals as a function of broad-band color $B-V$. The weighted mean velocity residual is $0.2 \pm 1.4\,{\rm km\,s^{-1}}$.

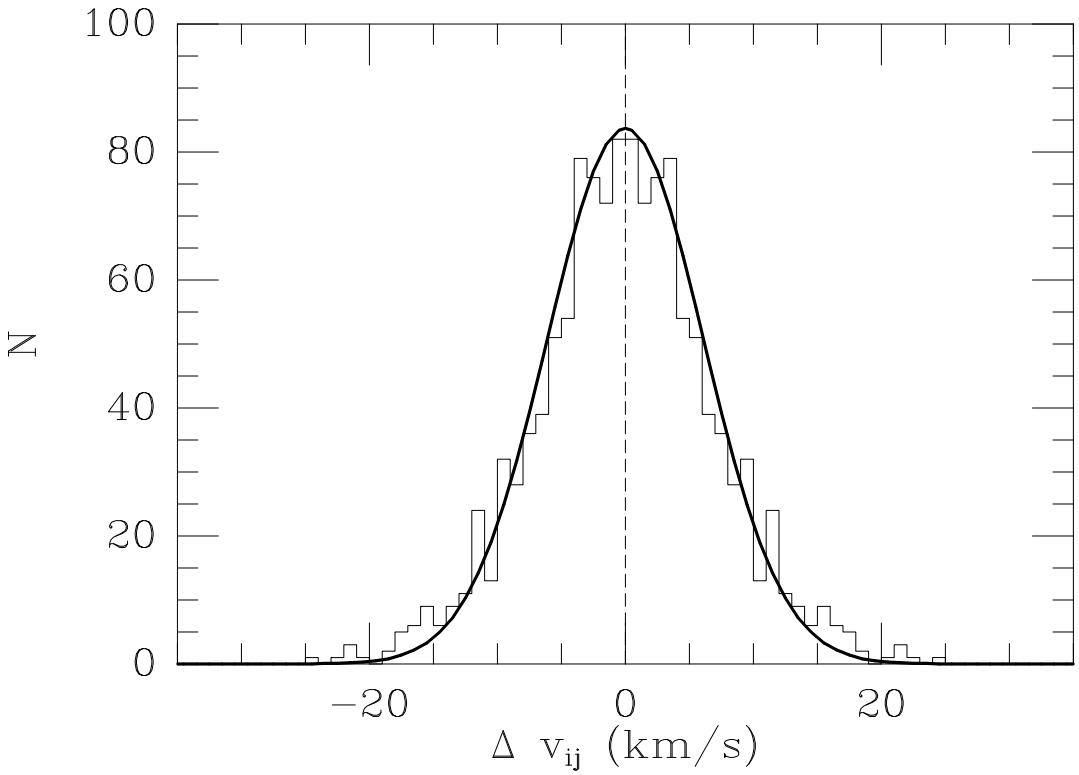

Fig. 8.— Histogram of the differences Δv_{ij} between multiple velocity measurements of the same star. The histogram includes those stars for which multiple independent STIS spectra are available that individually satisfy the selection criteria with respect to blending, S/N and $r_{\rm cc}$ discussed in the text. The histogram is well fit by a Gaussian with a dispersion of $6\,{\rm km\,s^{-1}}$ (solid curve). The stellar velocities themselves can be estimated with an uncertainty that is factor 2 smaller than this (because the statistical uncertainty in the average of two measurements is a factor 2 smaller than the statistical uncertainty in their difference).

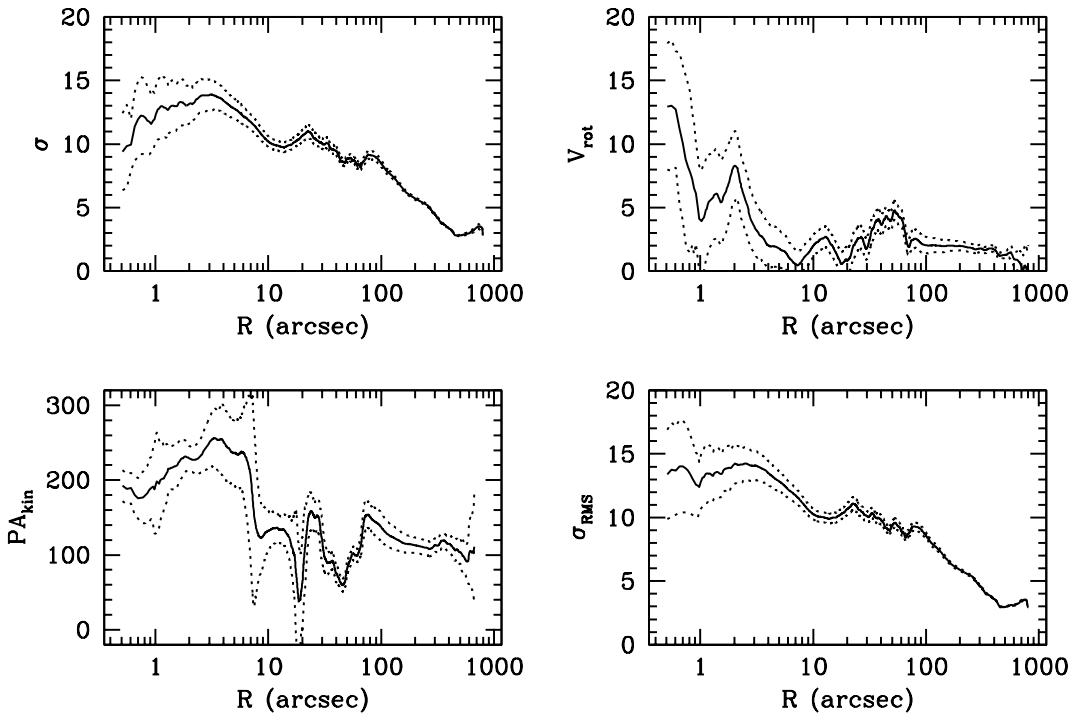

Fig. 9.— Radial profiles of projected kinematical quantities inferred from the combined HST/STIS and ground-based stellar line-of-sight velocity samples. **(a; top left panel)** Velocity dispersion σ; **(b; top right panel)** Rotation velocity $V_{\rm rot}$; **(c; bottom left panel)** Position angle $\mathrm{PA_{kin}}$ of the kinematical major axis; **(d; bottom right panel)** The RMS projected line-of-sight velocity $\sigma_{\rm RMS} \equiv \langle V_{\rm rot}^2 + \sigma^2 \rangle^{1/2}$, where the angle brackets denote the average over a ring on the projected plane of the sky. Solid curves are best estimates; dotted curves define the 68.3% confidence bands.

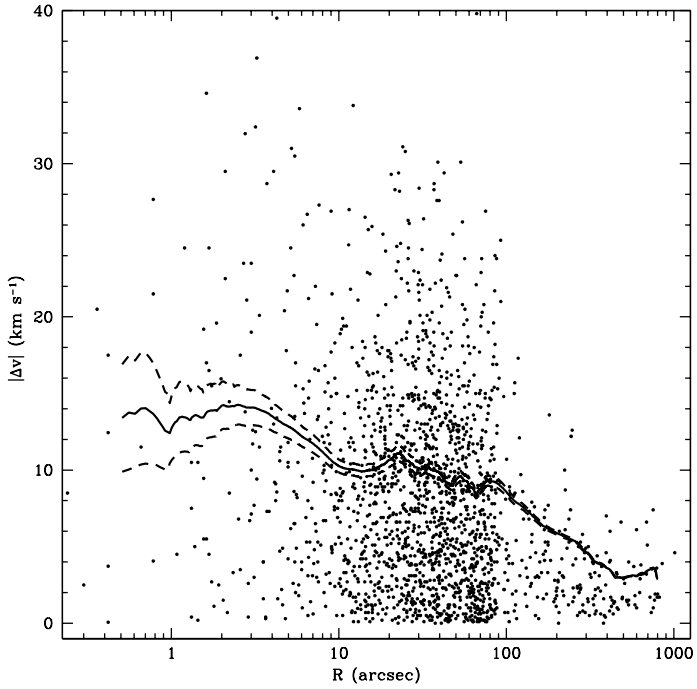

Fig. 10.— Curves show the radial profile of $\sigma_{\rm RMS}$ with its associated uncertainty, as in Figure 9d. For comparison, data points show the absolute value of the difference $\Delta v \equiv v_* - v_{\rm sys}$ between the measured velocities of individual stars and the M15 systemic velocity. This allows some visual assessment of the radial trends in the data. The $\sigma_{\rm RMS}$ curves start at $R = 0.5''$, which is the average radius of the innermost 11 data points (11 is the adopted data window size in `SROTATE`). The radial distribution of the data points reflects not only the distribution of stars in M15, but also observational selection bias.

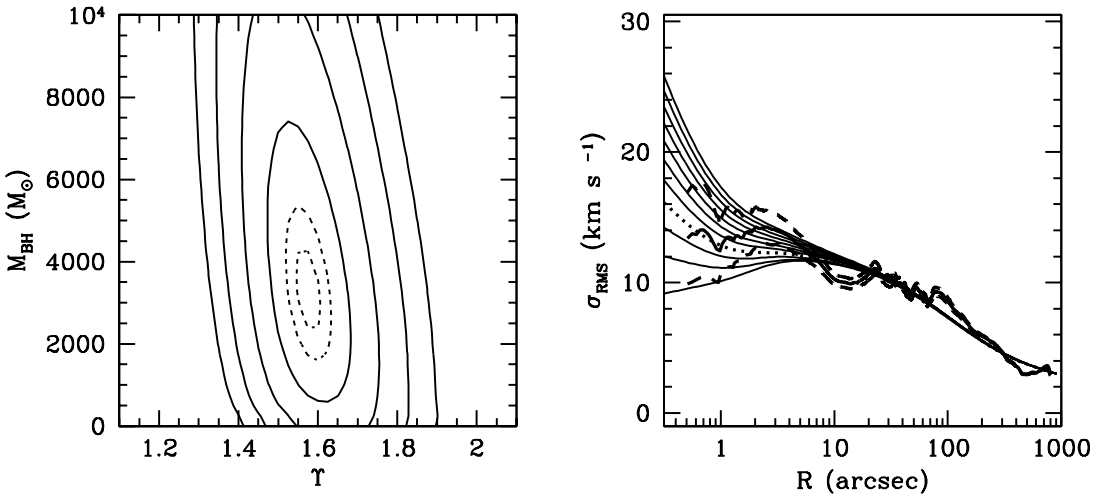

Fig. 11.— Data-model comparison for spherical dynamical models with an isotropic velocity distribution, a constant mass-to-light ratio Υ (in solar V-band units), and a central black hole of mass $M_{\rm BH}$. **(a; left panel)** Likelihood contours as function of Υ and $M_{\rm BH}$. The best-fit model has $\Upsilon = 1.6 \pm 0.1$ and $M_{\rm BH} = (3.2 \pm 2.2) \times 10^3\,{\rm M}_\odot$. Solid curves indicate the 1, 2, 3σ and 4σ confidence regions in the two-dimensional $(\Upsilon, M_{\rm BH})$ plane. Dotted curves show likelihood contours inside the 1σ region. **(b; right panel)** The RMS projected line-of-sight velocity $\sigma_{\rm RMS}$ as a function of projected radius R. The heavy jagged curve surrounded by heavy dashed curves is the observed profile, as in Figure 9d. The smooth thin curves are the predictions for models with $\Upsilon = 1.6$ and $M_{\rm BH}$ ranging from 0 to $10 \times 10^3\,{\rm M}_\odot$ in steps of $10^3\,{\rm M}_\odot$. The dotted curve highlights the predictions for $M_{\rm BH} = 3 \times 10^3\,{\rm M}_\odot$, which is closest to the best-fit value $M_{\rm BH} = (3.2 \pm 2.2) \times 10^3\,{\rm M}_\odot$.

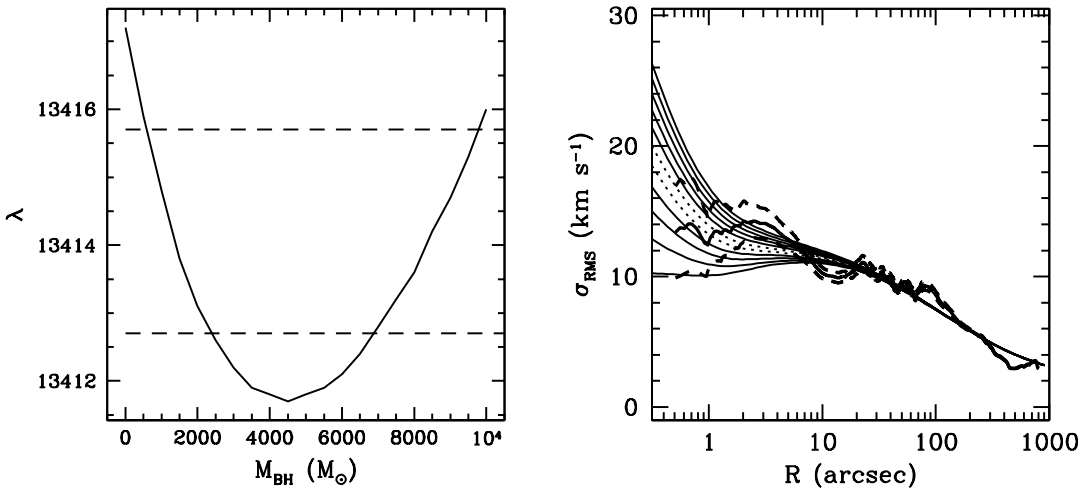

Fig. 12.— Data-model comparison for spherical dynamical models with an isotropic velocity distribution, a mass-to-light ratio profile $\Upsilon(r)$ inferred from Fokker-Planck models (Dull et al. 1997), and a central black hole of mass $M_{\rm BH}$. **(a; left panel)** The likelihood quantity λ defined in equation (4) as function of $M_{\rm BH}$. The minimum in λ identifies the best fit black hole mass. Horizontal dashed lines indicate the 1 and 2σ confidence regions. **(b; right panel)** The RMS projected line-of-sight velocity $\sigma_{\rm RMS}$ as a function of projected radius R. The heavy jagged curve surrounded by heavy dashed curves is the observed profile, as in Figure 9d. The smooth thin curves are the predictions for models with $M_{\rm BH}$ ranging from 0 to $10 \times 10^3\,{\rm M}_\odot$ in steps of $10^3\,{\rm M}_\odot$. The dotted curves highlight the predictions for $M_{\rm BH} = 4 \times 10^3\,{\rm M}_\odot$ and $M_{\rm BH} = 5 \times 10^3\,{\rm M}_\odot$, which bracket the best fit value $M_{\rm BH} = (4.5 \pm 2.1) \times 10^3\,{\rm M}_\odot$.

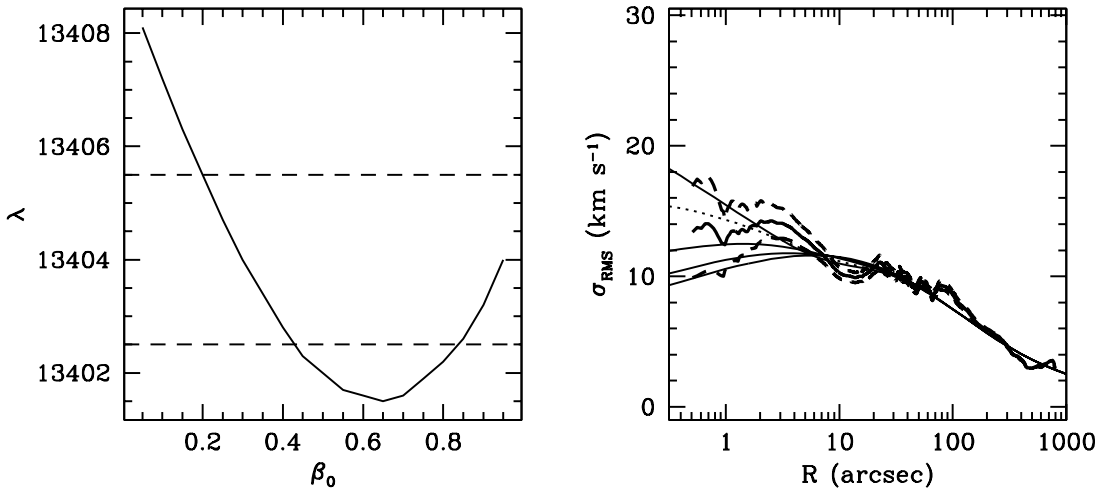

Fig. 13.— Data-model comparison for spherical dynamical models with an anisotropic velocity distribution parameterized by equation (6), a constant mass-to-light ratio Υ, and no central black hole. **(a; left panel)** The likelihood quantity λ defined in equation (4) as function of the central anisotropy β_0. At each β_0, the parameters a and Υ were varied to optimize the fit; β_∞ was kept fixed at zero. The minimum in λ identifies the best fit β_0. Horizontal dashed lines indicate the 1 and 2σ confidence regions. **(b; right panel)** The RMS projected line-of-sight velocity $\sigma_{\rm RMS}$ as a function of projected radius R. The heavy jagged curve surrounded by heavy dashed curves is the observed profile, as in Figure 9d. The smooth thin curves are the predictions for the best-fit models with $\beta_0 = 0$, 0.2, 0.4, 0.65 and 0.8. The dotted curve is for $\beta_0 = 0.65$, which provides the overall best fit. This indicates that considerable radial anisotropy must be invoked near the cluster center to explain the observations without invoking a central mass concentration.

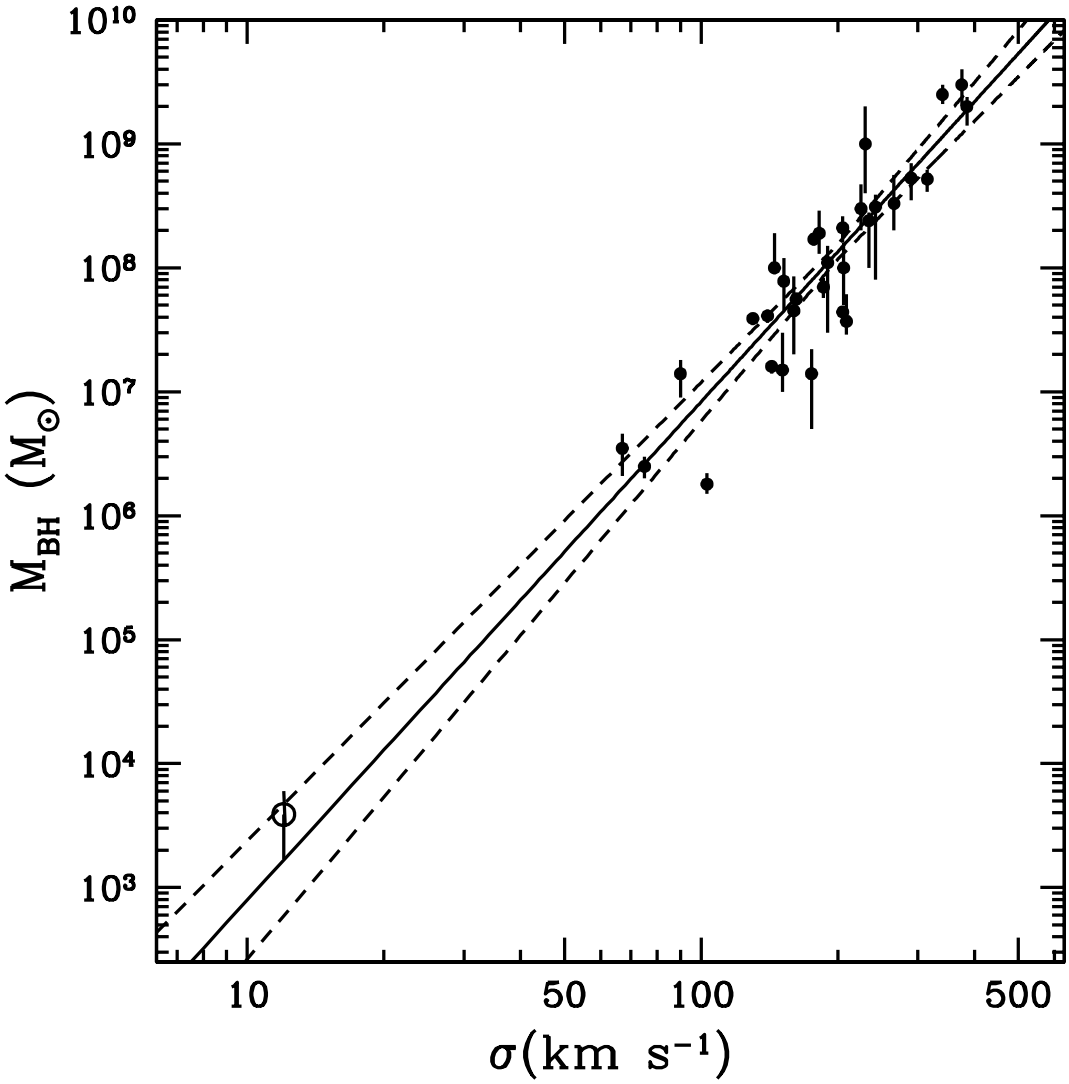

Fig. 14.— The black hole mass $M_{\rm BH}$ versus velocity dispersion σ. Solid points are measurements for various types of galaxies from the compilation of Tremaine et al. (2002). The solid line is the best linear fit, and the dashed lines show the 1σ confidence band. The black hole mass estimate for M15 obtained from isotropic models, $M_{\rm BH} = (3.9 \pm 2.2) \times 10^3\,{\rm M}_\odot$ (open point; this is the average of the masses inferred in Sections 5.3 and 5.4), fits perfectly onto the correlation.

Table 1. HST/STIS stellar velocity results

ID	Δ RA (arcsec)	Δ DEC (arcsec)	V	$B-V$	$v_{\rm obs}$ (km s^{-1})	$\Delta v_{\rm obs}$ (km s^{-1})	$r_{\rm cc}$	f	$v_\star$ (km s^{-1})	$\Delta v_\star$ (km s^{-1})	$v_{\rm ground}$ (km s^{-1})	$\Delta v_{\rm ground}$ (km s^{-1})
(1)	(2)	(3)	(4)	(5)	(6)	(7)	(8)	(9)	(10)	(11)	(12)	(13)
696	7.44	14.15	18.62	0.53	−102.7	5.0	2.06	0.836	−101.8	6.5		
824	6.90	13.95	17.83	0.71	−98.9	4.9	2.13	0.932	−98.3	5.3	−99.1	7.3
1299	6.28	11.93	19.05	0.48	−116.2	4.6	2.88	0.867	−117.6	5.6		
2341	4.21	8.76	17.45	0.71	−107.6	3.5	4.34	0.889	−107.6	4.2		
2357	4.34	8.51	14.99	0.80	−101.4	2.6	20.82	0.991	−101.4	2.6	−102.6	1.6
2703	3.95	7.23	13.51	1.11	−88.0	2.8	10.59	0.995	−87.9	2.8	−90.9	0.9
3393	2.82	5.66	15.86	0.29	−99.0	7.0	2.22	0.984	−98.9	7.1	−106.7	6.0
3726	2.38	4.91	18.03	0.69	−81.1	6.3	2.35	0.893	−77.9	7.2		
3798	2.52	4.48	17.62	0.71	−88.1	3.3	4.31	0.809	−83.5	5.0		
3911	2.32	4.36	15.32	0.85	−93.7	3.0	6.80	0.928	−92.6	3.3	−98.4	1.9
4185	1.48	4.24	18.41	0.61	−98.9	3.7	2.08	0.752	−96.0	6.3		
4768	0.95	2.86	17.63	0.69	−88.3	4.4	2.75	0.835	−84.5	5.7		
4891	0.77	2.65	17.50	0.68	−79.8	4.2	3.38	0.897	−76.6	4.9	−74.9	6.5
4908	0.95	2.40	18.50	0.57	−121.2	4.2	2.19	0.751	−125.7	6.9		
5002	1.18	1.84	15.02	0.77	−92.2	4.0	2.73	0.903	−90.5	4.6	−93.4	1.8
5003	1.49	1.53	16.60	0.71	−134.9	3.0	6.99	0.911	−137.5	3.5		
5029	1.21	1.72	17.10	0.70	−90.9	3.7	4.59	0.754	−85.5	6.2		
5031	0.92	2.02	17.83	0.79	−114.4	3.6	3.61	0.784	−116.3	5.7		
5222	0.31	1.98	17.77	0.67	−85.6	4.8	2.83	0.753	−78.4	7.5	−106.0	8.2
5263	0.74	1.35	17.03	0.74	−112.3	3.4	4.96	0.861	−113.0	4.4		
5304	0.46	1.54	17.53	0.66	−111.7	4.9	2.09	0.753	−113.1	7.6		
5380	0.08	1.70	17.48	0.68	−88.6	5.3	2.48	0.778	−83.2	7.6		
5515	−0.21	1.59	17.24	0.61	−117.4	4.3	3.40	0.799	−119.9	6.1	−115.8	5.0
5755	−0.17	0.76	17.48	0.62	−124.0	7.9	2.20	0.765	−129.1	11.0		
5768	0.37	0.18	15.22	0.86	−105.8	4.1	3.52	0.854	−105.5	5.2	−108.2	3.2
5785	0.07	0.44	17.02	0.76	−109.9	3.1	6.79	0.753	−110.7	5.7		
5831	0.36	−0.03	15.10	0.70	−124.3	2.7	12.53	0.797	−128.6	4.6	−116.5	3.4
5846	0.40	−0.11	15.49	0.34	−70.2	3.7	4.24	0.755	−58.1	6.3		
5864	−0.72	1.00	17.61	0.53	−126.9	4.0	2.55	0.765	−132.9	6.4		
5926	−0.10	0.19	16.61	0.26	−101.3	3.4	4.15	0.799	−99.8	5.3		
5933	−0.51	0.58	14.55	0.82	−81.8	2.6	17.68	0.934	−79.9	2.9	−79.9	1.1
6005	−0.38	0.21	16.89	0.57	−94.2	3.7	3.88	0.791	−90.6	5.7		
6012	−0.27	0.08	16.88	0.68	−109.7	3.3	5.85	0.761	−110.4	5.7		
6044	−0.61	0.31	17.66	0.60	−98.9	4.9	2.49	0.759	−96.2	7.6		
6111	−0.16	−0.35	17.49	0.72	−92.0	3.5	4.04	0.761	−87.1	5.9		
6290	−0.47	−0.57	13.71	1.01	−104.2	2.5	35.00	0.984	−104.2	2.6	−103.4	1.0
6433	−1.31	−0.16	17.19	0.45	−99.0	3.7	3.37	0.820	−97.1	5.2		
6450	−0.68	−0.83	16.90	0.01	−111.2	4.7	2.11	0.752	−112.4	7.4		
6575	−0.85	−1.04	17.33	0.62	−113.7	3.5	4.82	0.786	−115.3	5.5		
6617	−1.26	−0.73	17.33	0.73	−117.0	4.3	4.04	0.846	−118.7	5.5		
6711	−1.52	−0.75	17.57	0.74	−95.1	6.5	2.02	0.779	−91.6	9.0		
6719	−0.92	−1.37	17.95	0.75	−104.2	3.8	2.87	0.780	−103.2	6.0		
6772	−1.23	−1.25	14.86	0.88	−101.0	2.7	11.57	0.949	−100.6	2.9	−109.3	2.6
6828	−0.72	−1.92	17.64	0.63	−109.4	5.2	2.00	0.830	−109.7	6.8		
6833	−1.18	−1.47	15.84	0.84	−129.9	2.9	9.86	0.856	−133.7	3.9	−122.5	4.1
7148	−2.00	−1.64	17.05	0.70	−111.4	3.4	4.43	0.913	−111.8	3.9		
7313	−2.02	−2.19	15.40	0.73	−99.1	2.9	8.79	0.928	−98.4	3.3	−102.1	3.5
7404	−1.74	−2.78	16.40	0.72	−97.9	3.1	6.34	0.958	−97.5	3.3	−100.7	6.4
7656	−1.36	−4.00	17.38	0.66	−93.0	3.9	2.64	0.831	−90.0	5.3	−102.3	3.6
7718	−2.39	−3.14	14.23	0.97	−92.8	2.6	23.41	0.991	−92.6	2.6	−93.7	1.4
7775	−2.05	−3.76	17.65	0.66	−142.2	4.8	3.41	0.876	−147.2	5.8		
8146	−1.89	−5.19	17.30	0.16	−120.5	4.1	2.08	0.833	−123.1	5.5		
8194	−3.09	−4.13	15.61	0.85	−103.3	2.7	11.20	0.975	−103.2	2.8	−100.7	2.3
8260	−3.10	−4.41	17.33	0.69	−102.6	3.9	3.89	0.851	−101.7	5.0		
8292	−3.04	−4.57	17.57	0.66	−102.7	8.5	2.27	0.824	−101.7	10.6		
8362	−2.91	−4.93	18.22	0.62	−115.9	4.3	2.09	0.787	−118.2	6.3		
8396	−3.13	−4.83	17.28	0.67	−105.5	3.4	4.07	0.907	−105.3	3.9		
8492	−3.31	−4.97	17.60	0.00	−111.5	4.9	2.12	0.909	−111.9	5.6		
8496	−2.86	−5.45	16.46	0.74	−95.8	3.0	6.72	0.941	−95.1	3.3	−92.0	3.2
8760	−2.86	−6.38	17.72	0.75	−96.6	3.8	4.05	0.863	−94.9	4.8		
8917	−3.14	−6.68	16.84	0.70	−89.8	3.9	2.41	0.933	−88.5	4.3		
10602	−6.73	−11.08	15.39	0.82	−106.8	2.7	13.06	0.996	−106.8	2.7	−106.7	2.0
14442	11.48	22.89	17.48	0.68	−109.5	4.7	3.19	0.990	−109.5	4.7		
14526	12.07	24.37	15.12	0.87	−114.1	2.7	13.37	0.999	−114.2	2.7	−107.3	2.0

Note. — The ID number in column (1) corresponds to the number in the M15 stellar catalog presented in Paper I. The stellar positions [column (2) and (3)], V-band magnitudes [column (4)] and $B-V$ colors [column (5)] are taken from this catalog. The line-of-sight velocities inferred from the STIS spectra, and their uncertainties, are listed in columns (6) and (7), respectively. The $r_{\rm cc}$ cross-correlation statistic associated with the inferred velocity (see Section 2) is listed in column (8). The quantity f in column (9) measures the amount of blending in the spectrum (see Section 3.3). The blending corrected velocities and their errors are shown in columns (10) and (11). Ground-based velocity determinations and their associated errors, from the compilation of Gebhardt et al. (2000a), are listed in columns (12) and (13). Ground-based velocity determinations with uncertainties in excess of 10 km s^{-1} were omitted (these were available for stars 5785 and 8760).